Supplementary information

Closed-loop upcycling of protein amyloid fibrils from food waste for atmospheric CO_2 capture

Zhou Dong[1], Ming Dai[1,2], Felix Donat[3], Dominik Richert[3], Bin Dai[4], Jiangtao Zhou[5], Milad Radiom[1], Mohammad Peydayesh[1], Yanwen Li[1], Xiuhuai Li[6], Hui Wu[6], Christoph R. Müller[3], Wenshuai Chen[2], Raffaele Mezzenga[1,7*]

[1] *ETH Zürich, Department of Health Sciences and Technology, 8092 Zürich, Switzerland*

[2] *Key Laboratory of Bio-based Material Science and Technology, Ministry of Education, Northeast Forestry University, Harbin 150040, P.R. China*

[3] *ETH Zürich, Department of Mechanical and Process Engineering, Leonhardstrasse 21, CH-8092 Zürich, Switzerland*

[4] *School of Sensing Science and Engineering, School of Electronic Information and Electrical Engineering, Shanghai Jiao Tong University, Shanghai 200240, P.R. China*

[5] *Department of Food Science and Technology, National University of Singapore, Singapore*

[6] *College of Food Science and Engineering, South China University of Technology, Guangzhou 510640, P.R. China*

[7] *ETH Zürich, Department of Materials, 8093 Zürich, Switzerland*

[*] Corresponding author

E-mail: raffaele.mezzenga@hest.ethz.ch

Table of Contents

Section 1. Design Rationale Information

1.1 Circular DAC strategy based on food waste.

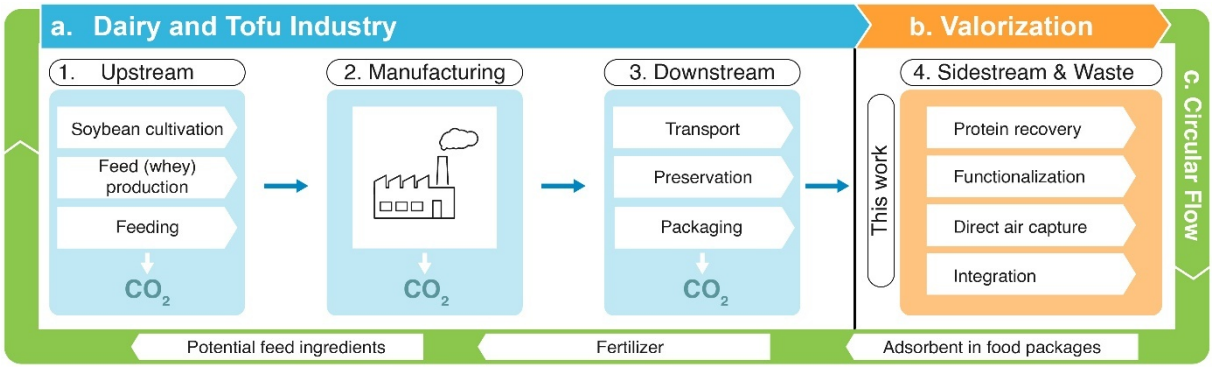

Supplementary Fig. 1 | Illustration of the circular DAC strategy. a, Carbon-intensive sections across dairy and tofu production chains, highlighting upstream (feed production and farming), manufacturing, and downstream (distribution, preservation, and packaging) emissions. Proposed closed-loop pathway that valorizes protein waste into CO_2 capture sorbents (**b**), followed by food system reintegration through application in food packages, potential feed ingredient, or fertilizer (**c**).

1.2 Ocean-inspired design rationale

The direct ocean capture system exploits the bicarbonate-carbonate equilibrium dynamics in seawater to facilitate CO_2 sequestration[1,2] (**Supplementary Fig. 2**). Upon dissolution, atmospheric CO_2 forms carbonic acid (H_2CO_3), which rapidly dissociates into bicarbonate (HCO_3^-) and hydrogen ions at typical oceanic pH ranges (~pH 8). This dissociation drives the neutralization reaction within the alkalinity pool, which is primarily composed of bicarbonate and carbonate ions (CO_3^{2-}), serving as the system's buffering capacity. In the presence of calcium ions (Ca^{2+}), carbonate ions combine to form calcium carbonate ($CaCO_3$). This carbon fixation process is often facilitated by marine organisms, such as coccolithophores, corals, and shellfish, which utilize $CaCO_3$ to build their shells and skeletons. The regeneration of the alkalinity pool involves the dissolution of calcium carbonate ($CaCO_3$), releasing carbonate ions back into solution. This mineralization-dissolution cycle maintains system alkalinity while permanently sequestering captured CO_2.

In our alkaline-amyloid fibril system, the KOH (an alkalinity pool) reacts with CO_2 to form bicarbonate, and the amyloid fibrils with rich amine groups (analogous to marine organisms) have a similar function to $CaCO_3$ in fixing the bicarbonate (**Supplementary Fig. 3**).

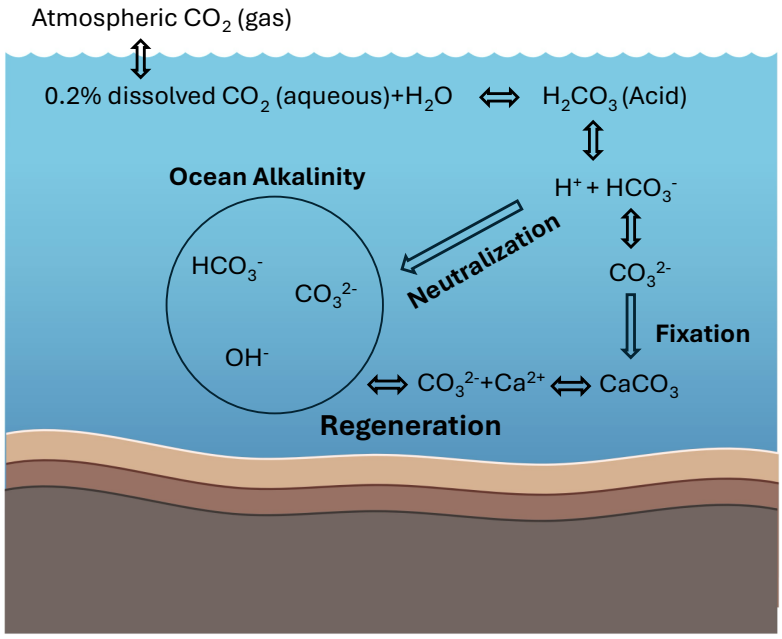

Supplementary Fig. 2 | The thermal-free CO_2 capture, fixation, and regeneration process by the ocean.

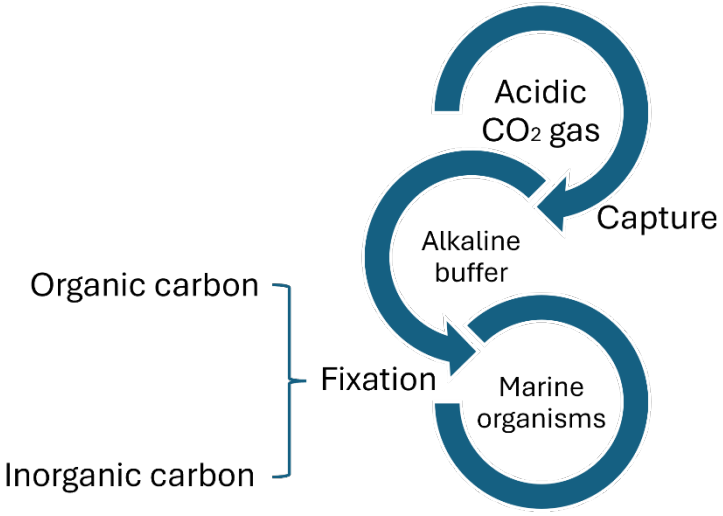

Supplementary Fig. 3 | Carbon capture and fixation by alkaline buffer system and marine organisms.

1.3 Challenges in hydroxide-based sorbents

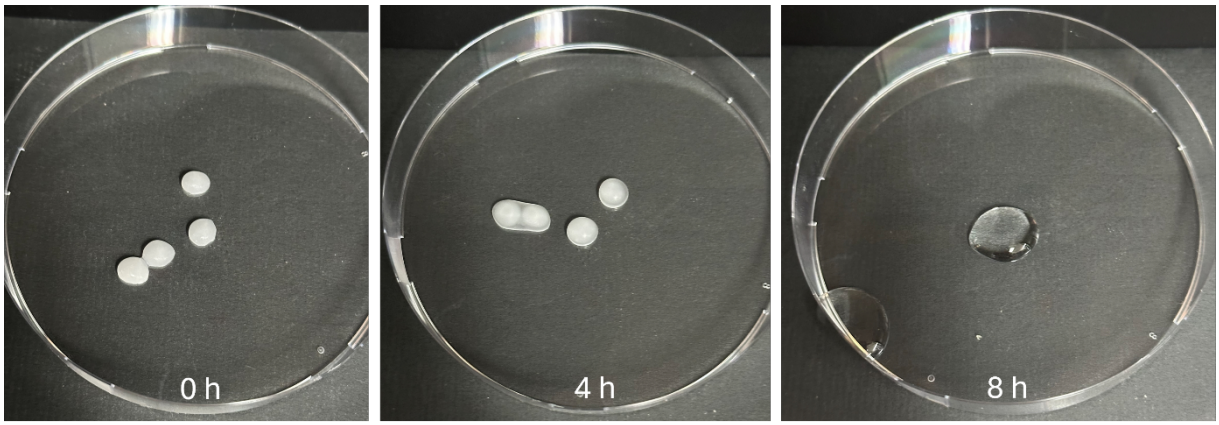

Supplementary Fig. 4 | Deliquescence of KOH pellet at ambient air under 40–50% RH at 25 °C after 4-h and 8-h exposure.

Section 2. Small-Angle X-Ray Scattering (SAXS)

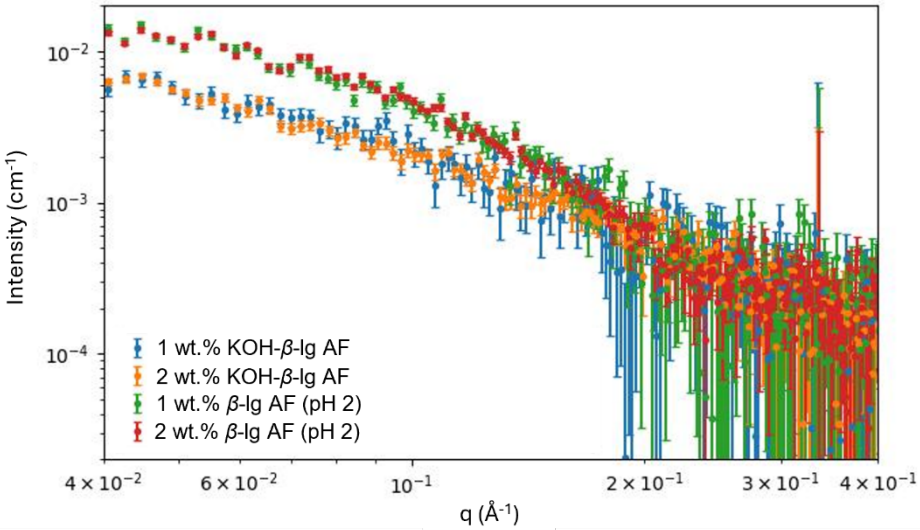

Supplementary Fig. 5 | Normalized SAXS spectra of 1 wt% and 2 wt% *β*-lg AFs at pH 2 and pH 12–13. 2 wt% *β*-lg AF was mixed with 1 M KOH at a 5:1 mass ratio and incubated for 7 days before measurement. 1 wt% *β*-lg AF solution at pH 12–13 was prepared by diluting the 2 wt% solution with distilled water at pH 12.

Supplementary Table 1 | Geometrical parameters of the AF at pH 2 and 12–13 based on fitting SAXS spectra to cylindrical form factor. To improve the fitting results, a similar diameter was assumed.

Fit parameters	Length (nm)	Diameter (nm)
pH 2.0	~7400	~2.6
pH (KOH)	~950	~2.6

Section 3. Transmission Electron Microscopy (TEM)

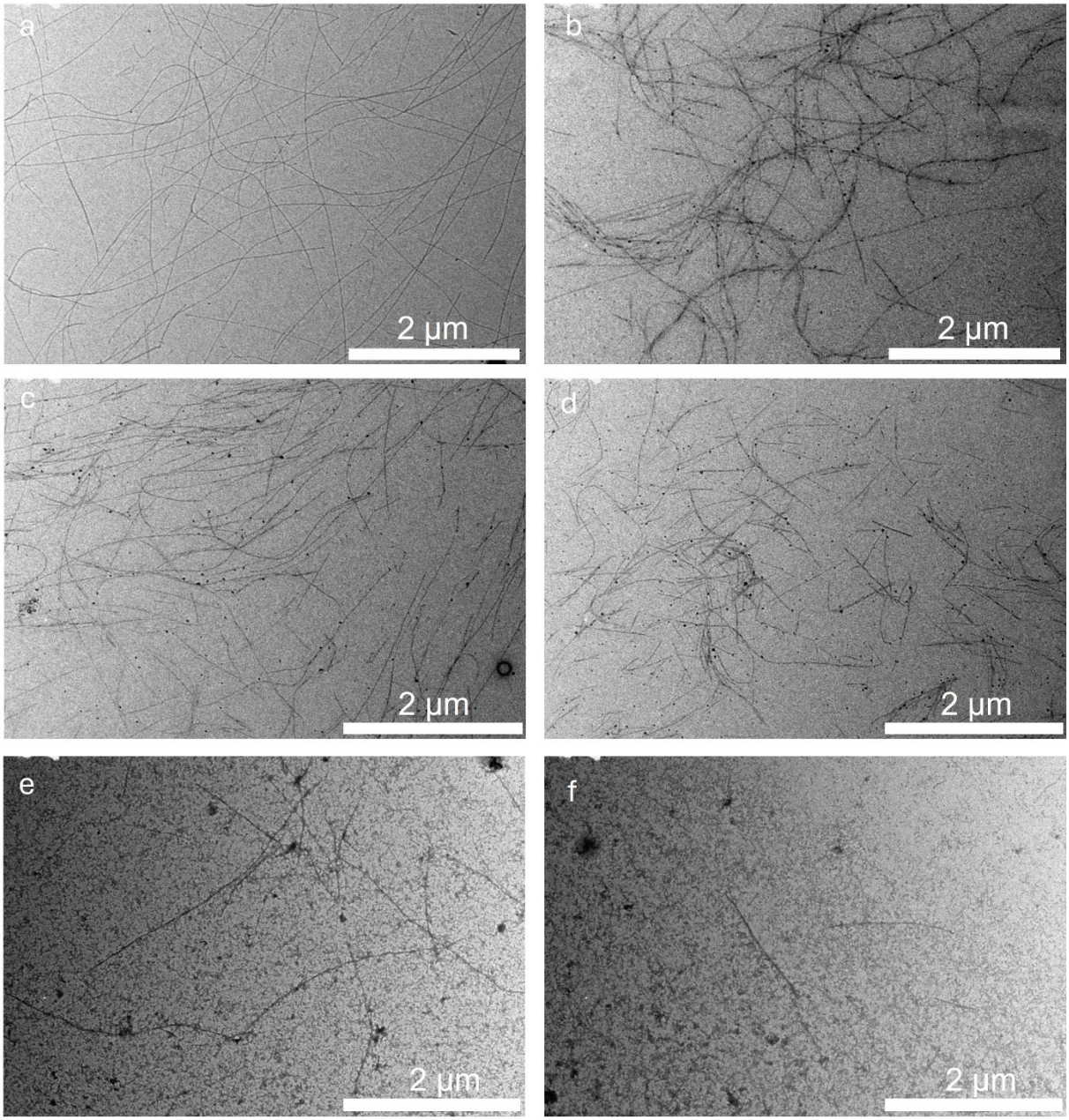

Supplementary Fig. 6 | TEM images of *β*-lg AF at pH 2 (a) and KOH-*β*-lg AF after 7-day (b) and 2-month incubation (c,d); SPI AF at pH 2 (e) and KOH-SPI AF after 7-day incubation (f). The scale bar is 2 μm. The images are representative of three technical replicates (n = 3), each yielding similar results.

Section 4. Atomic Force Microscopy (AFM)

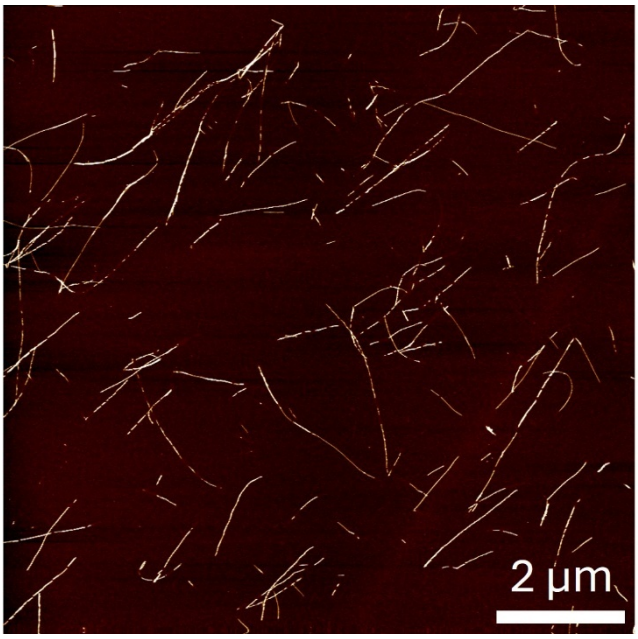

Supplementary Fig. 7 | AFM images of KOH-*β*-lg AF after 2-month incubation. The scale bar is 2 µm. The images are representative of three technical replicates (n = 3), each yielding similar results.

Section 5. Synthesis of Microbeads

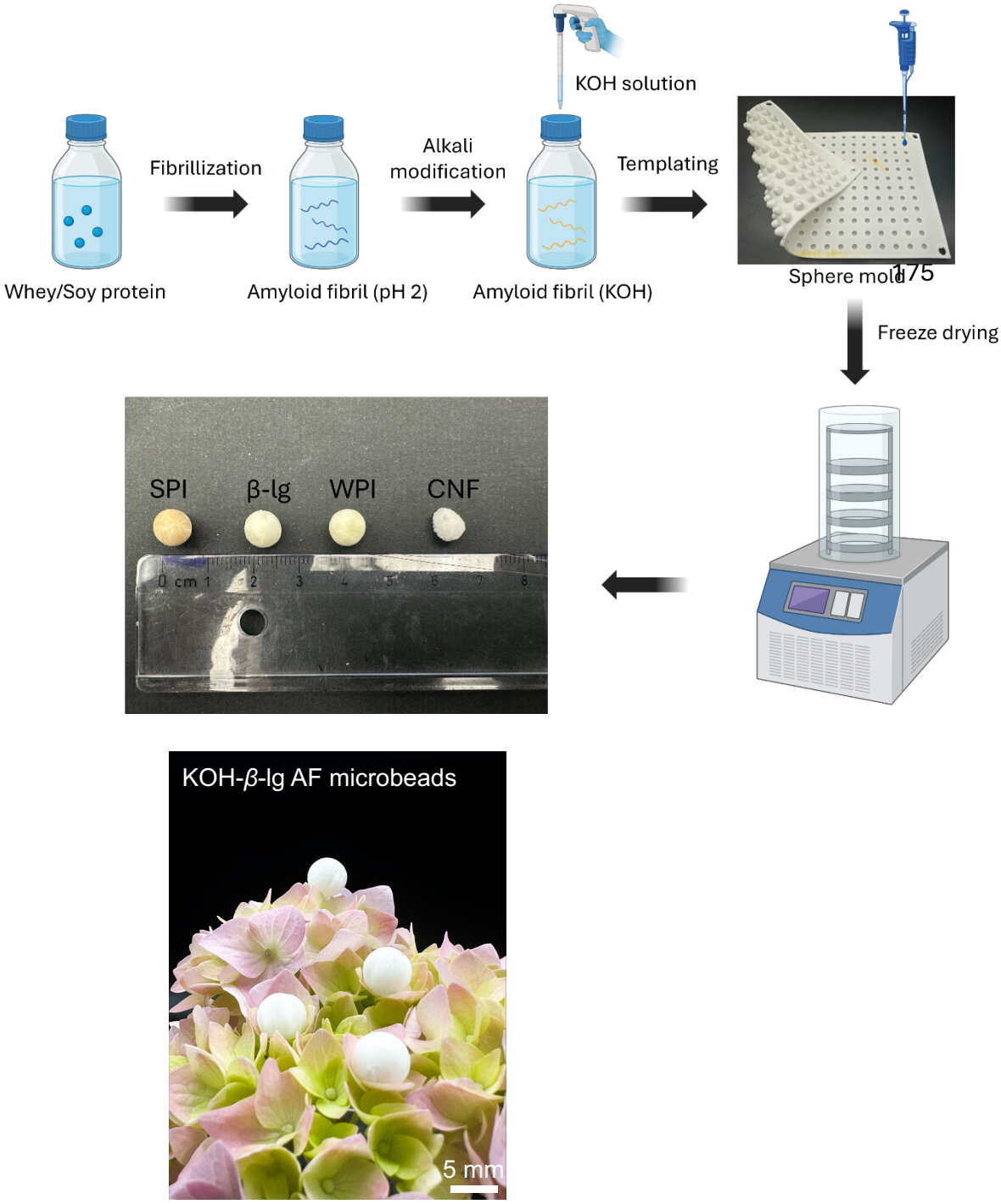

Supplementary Fig. 8 | Schematic of the synthesis of KOH-AF microbeads using SPI, *β*-lg, WPI, and CNF by sphere mold templating. *β*-lg AF (3 wt%), WPI AF (5 wt%), SPI AF (4 wt%), and WPI monomer (5 wt%) solutions at pH 2 were mixed with concentrated KOH solution (2 M) at a dry mass ratio of 5:1 mass for *β*-lg AF, WPI AF, and WPI monomer, and 10:1 for SPI AF. The color of KOH-*β*-lg and WPI AF microbeads gradually turned from white to yellow under prolonged storage in a sealed container (1–10 weeks). Scale bar, 5 mm.

Section 6. Scanning Electron Microscopy (SEM)

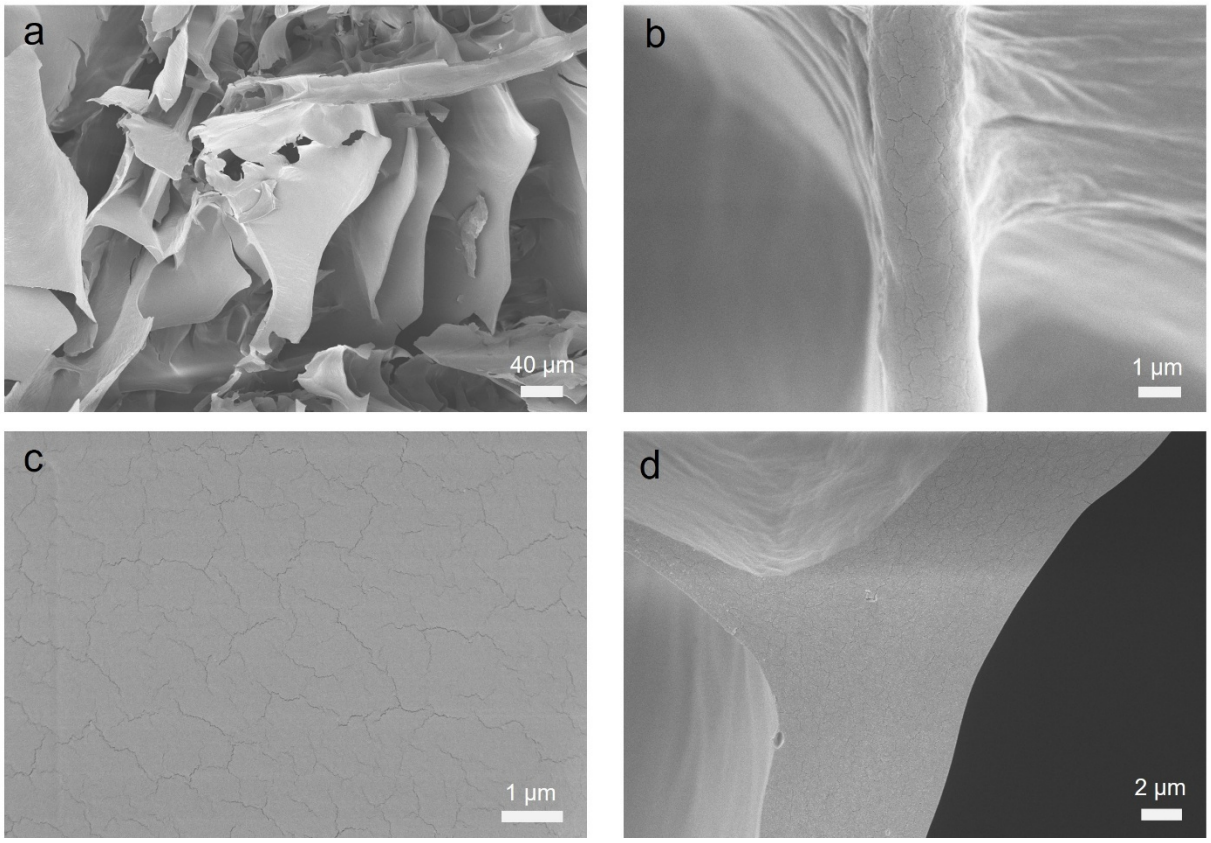

Supplementary Fig. 9 | SEM images of surface (a–c) and cross-section (d) of unmodified *β*-lg AF microbeads.

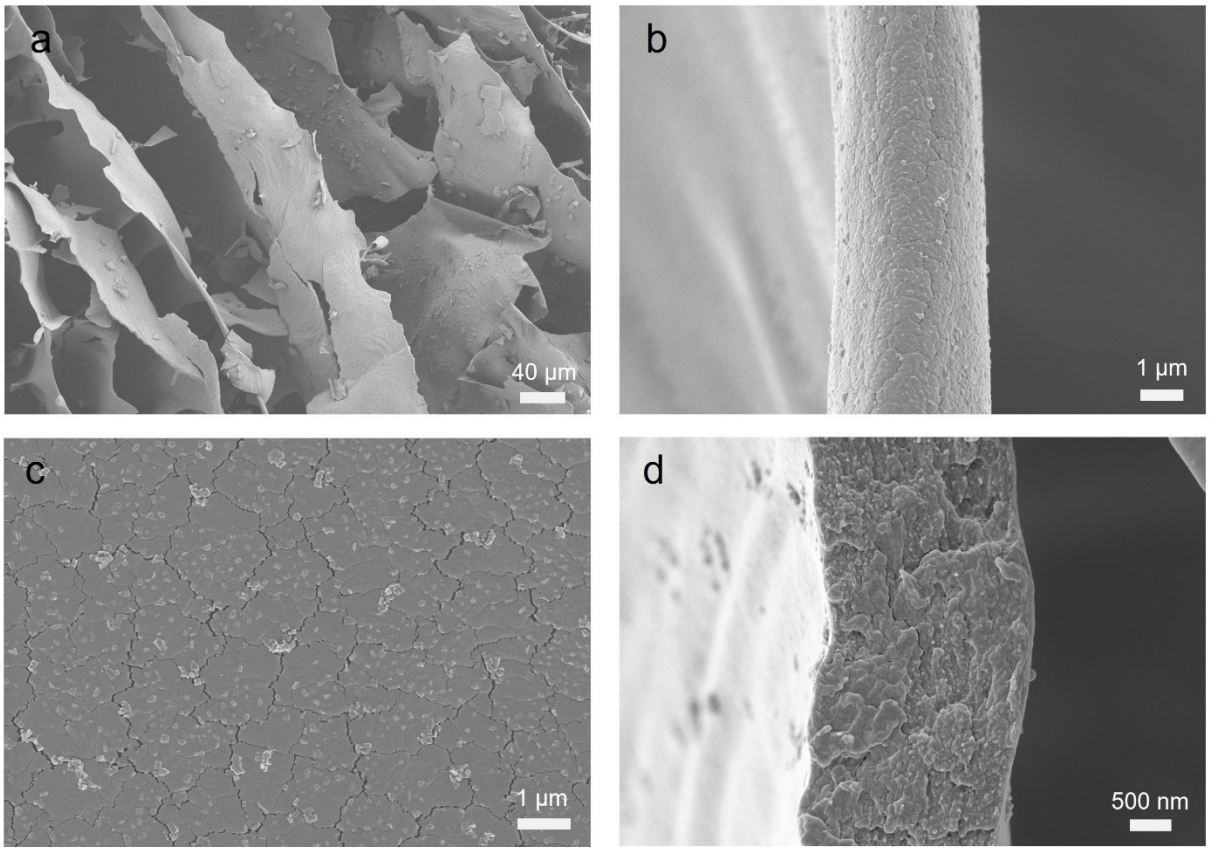

Supplementary Fig. 10 | SEM images of surface (a–c) and cross-section (d) of KOH-modified *β*-lg AF microbeads. The microbeads were stored in a sealed vial for 2 weeks before measurement, showing the stability of AF microbeads under prolonged alkaline exposure.

Section 7. Dry Ice Vapor Sorption

Supplementary Fig. 11 | The syringe pump for the generation of dry ice smoke with controlled flow direction and rate. 1 g of solid dry ice was mixed with 4 ml of distilled water inside the syringe. The flow rate was 420 ml h^{-1}.

Section 8. Single-Component Water Vapor Sorption Measurements

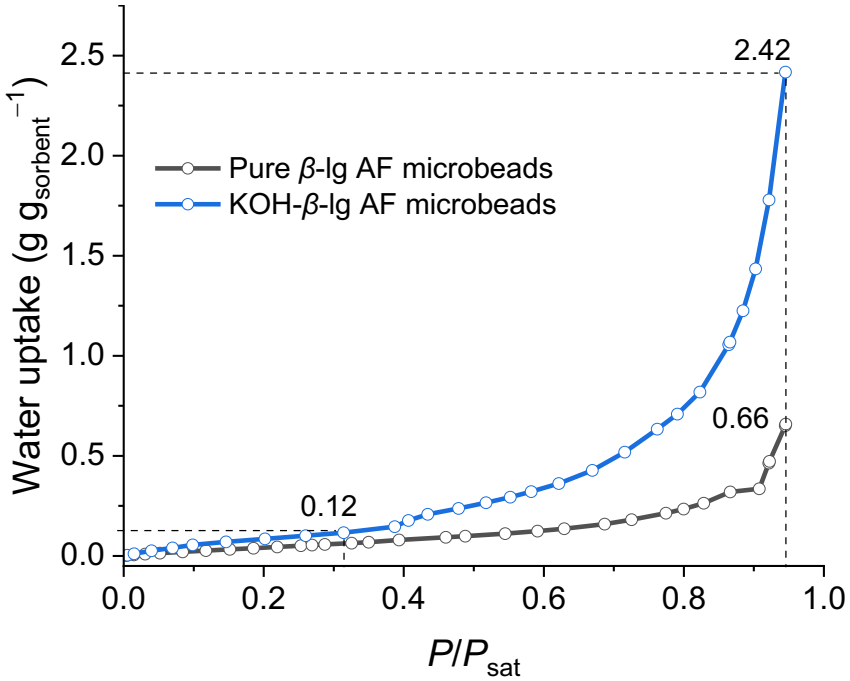

Supplementary Fig. 12 | Single-component water vapor sorption isotherm measured at 25 °C. P is water vapor pressure, and P_{sat} is the saturation water vapor pressure.

Section 9. Instrument for Dynamic Breakthrough Measurements

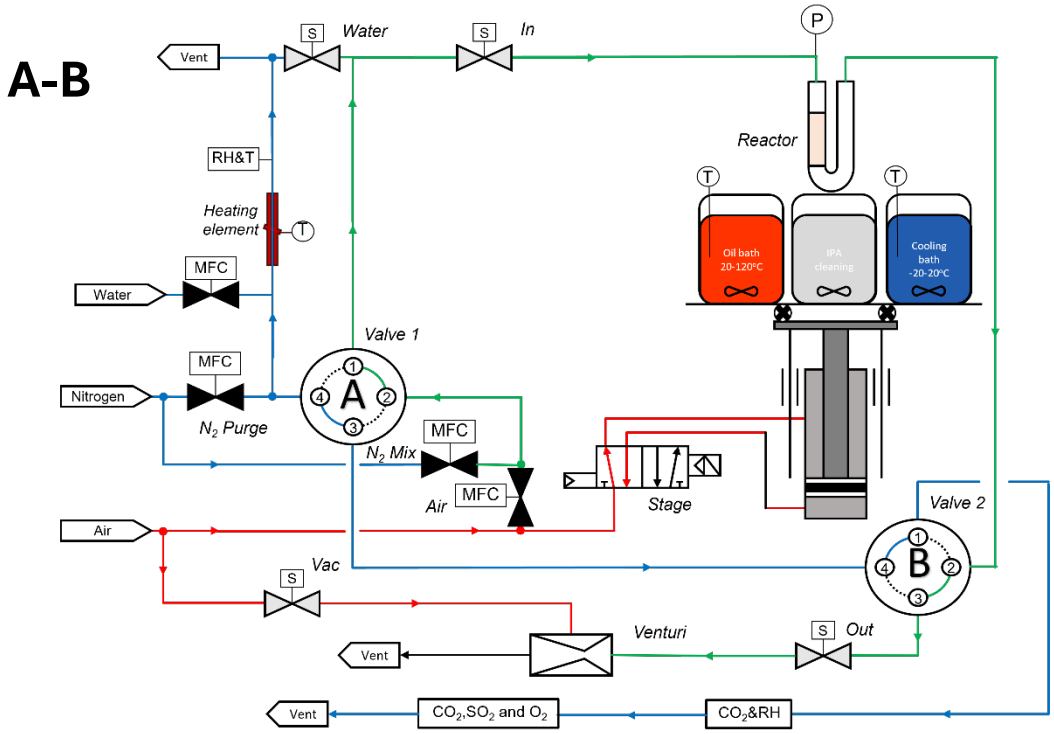

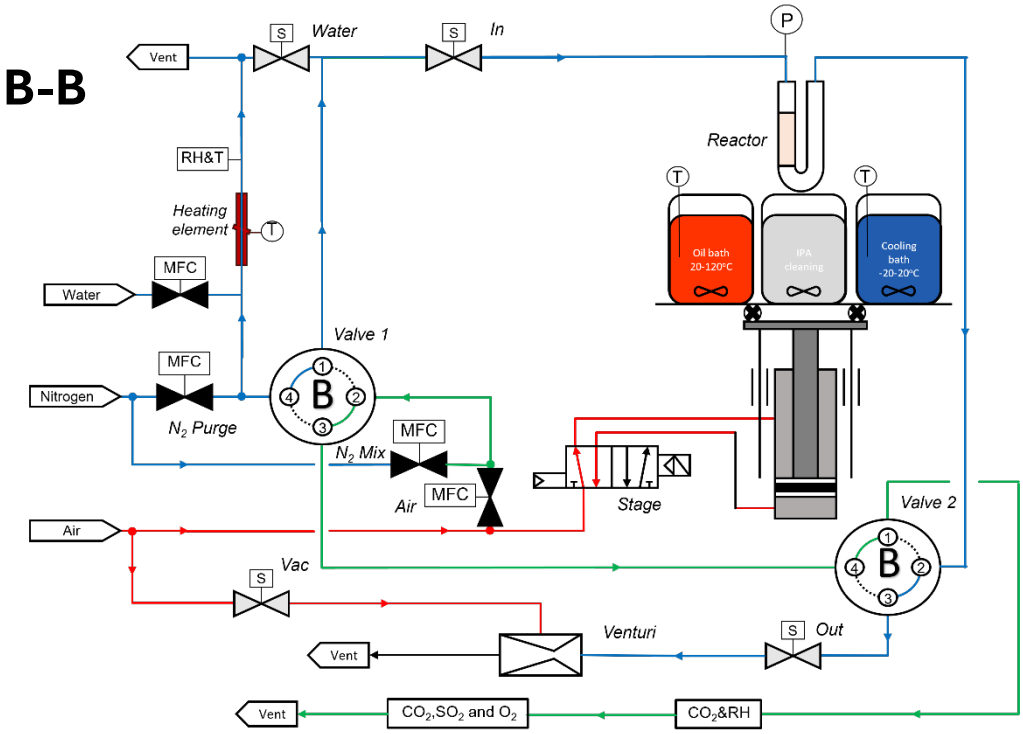

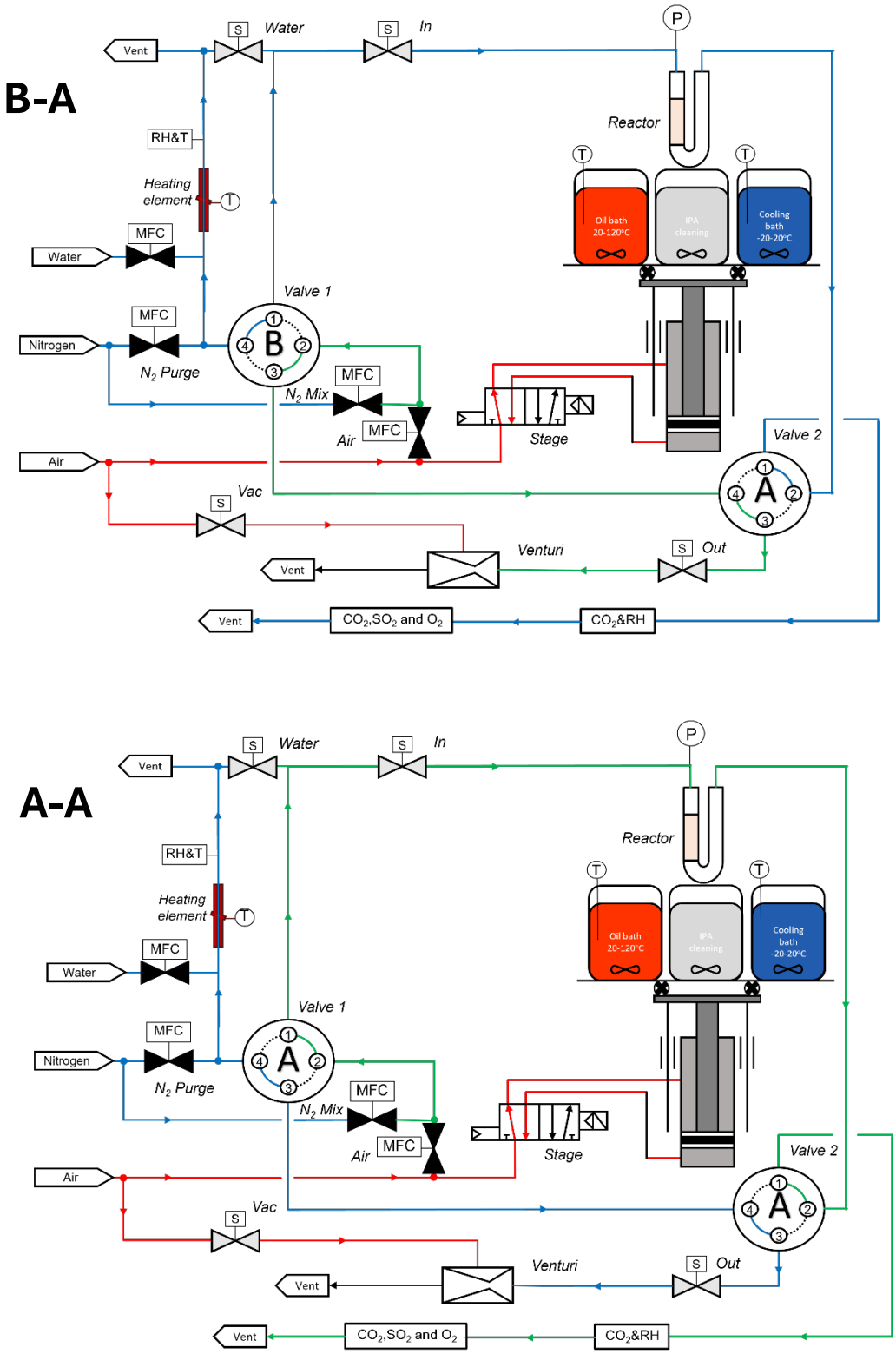

Supplementary Fig. 13 | Schematic diagram of the dynamic breakthrough measurement instrument.

Supplementary Table 2 | Function of valves in the dynamic breakthrough measurement instrument

Valve	Position	Effect
1	A	Gas mix to reactor, purge to bypass
	B	Purge to reactor, gas mix to bypass
2	A	Reactor gas to analyzers, bypass to venturi
	B	Reactor gas to venturi, bypass to analyzers

Section 10. Dynamic Breakthrough Measurements

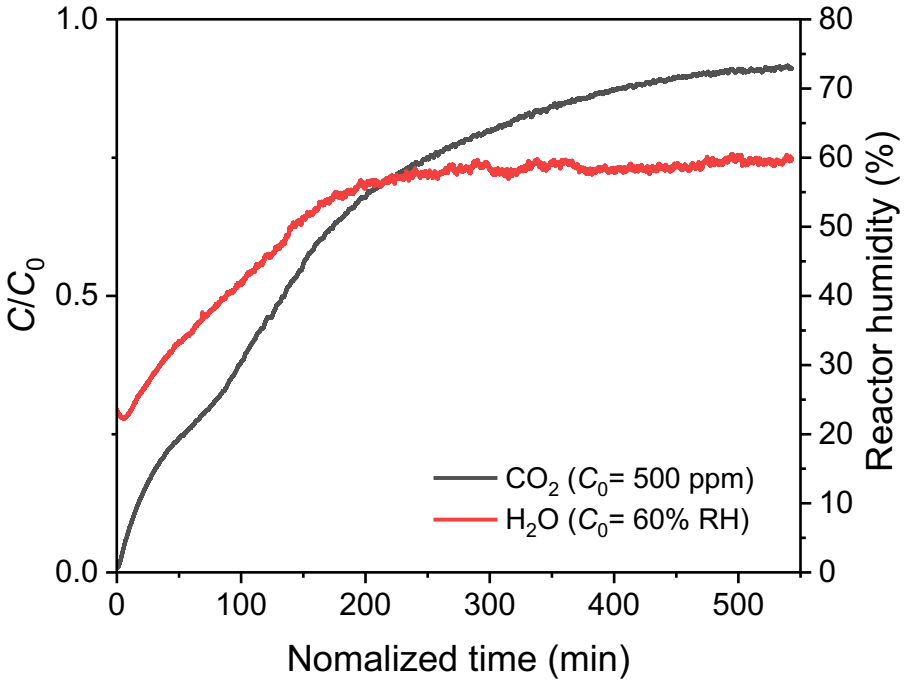

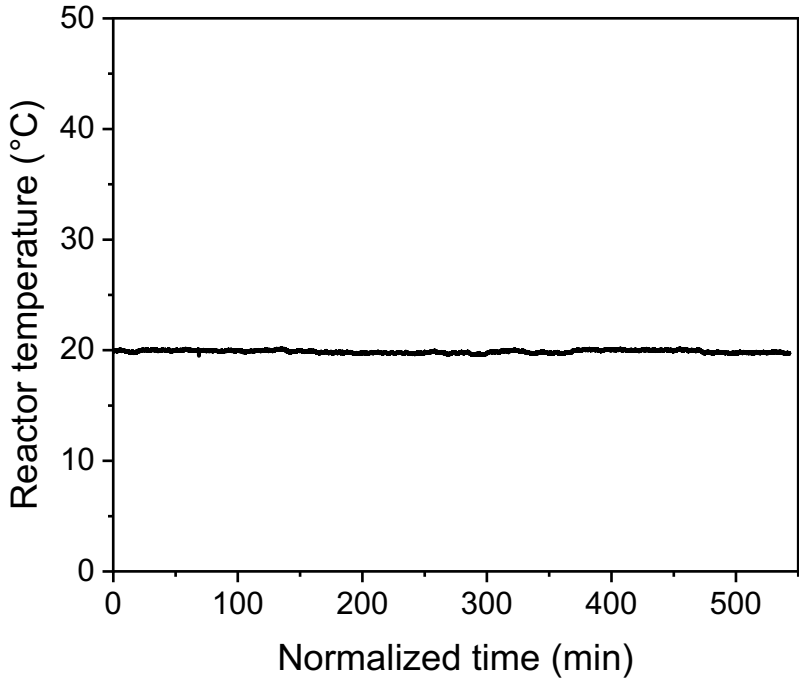

Supplementary Fig. 14 | Dynamic breakthrough measurements of KOH-WPI AF microbeads using simulated air (500 ppm of CO_2 balanced in N_2 with 60% RH) at 20 °C. 100 ± 10 mg of microbeads were degassed at 90 °C for 30 min in N_2, cooled down by methanol, and then prehumidified for 10 min before exposure to air.

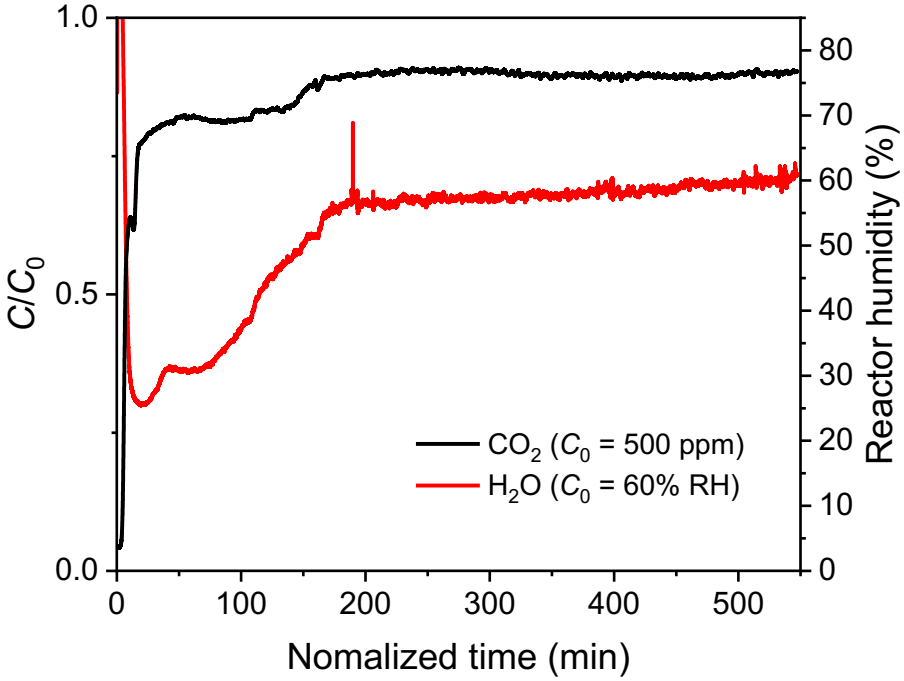

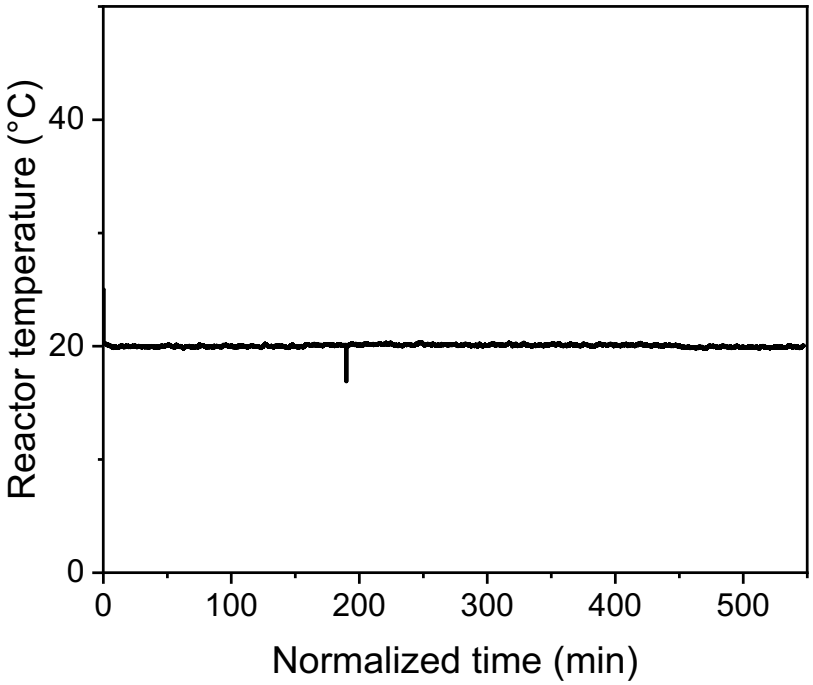

Supplementary Fig. 15 | Dynamic breakthrough measurements of KOH-SPI AF microbeads using simulated air (500 ppm of CO_2 balanced in N_2 with 60% RH) at 20 °C. 100 ± 10 mg of microbeads were degassed at 90 °C for 30 min in N_2, cooled down by methanol, and then prehumidified for 10 min before exposure to air.

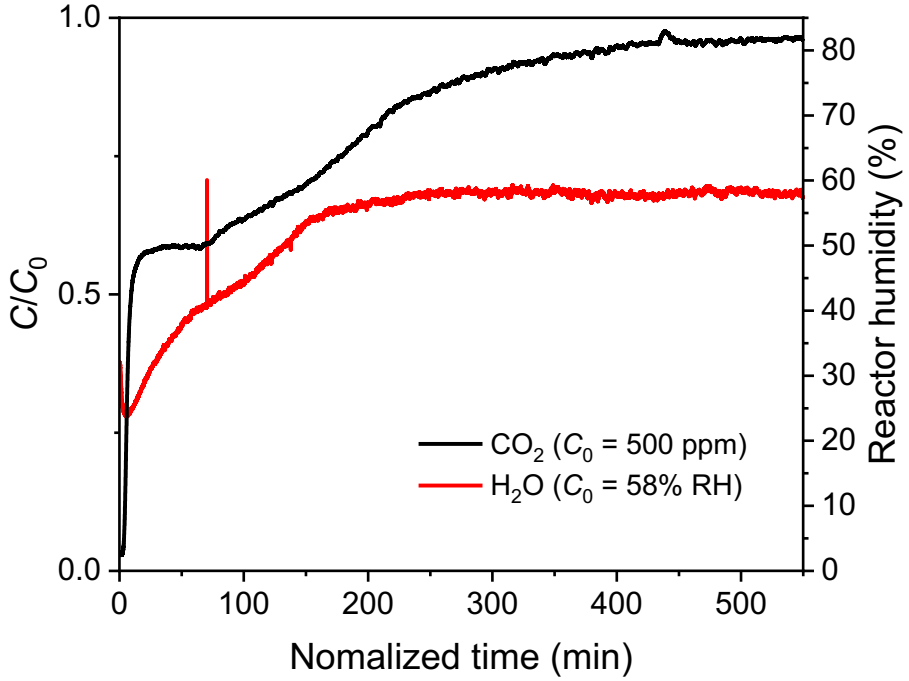

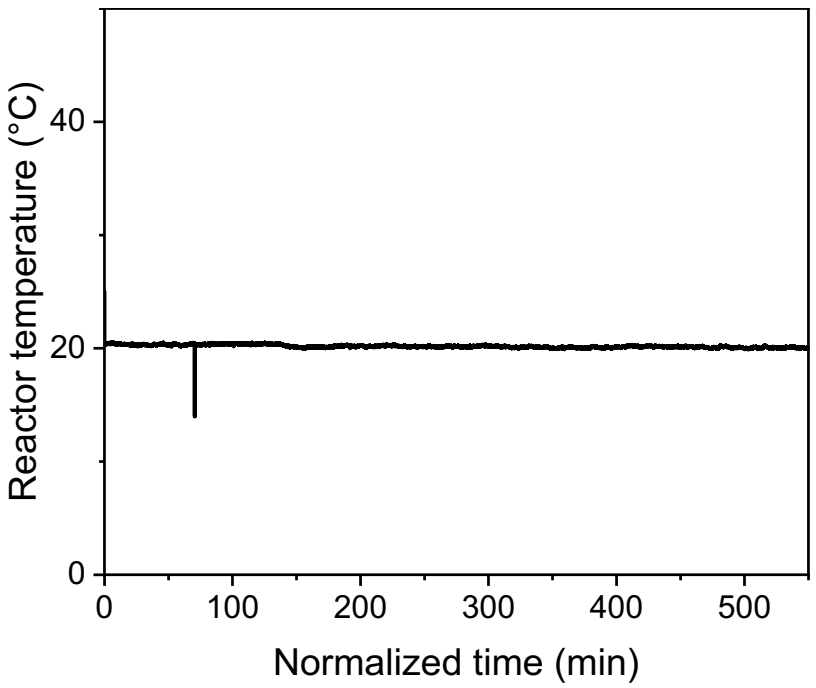

Supplementary Fig. 16 | Dynamic breakthrough measurements of KOH-WPI monomer microbeads using simulated air (500 ppm of CO_2 balanced in N_2 with 58% RH) at 20 °C. 100 ± 10 mg of microbeads were degassed at 90 °C for 30 min in N_2, cooled down by methanol, and then prehumidified for 10 min before exposure to air.

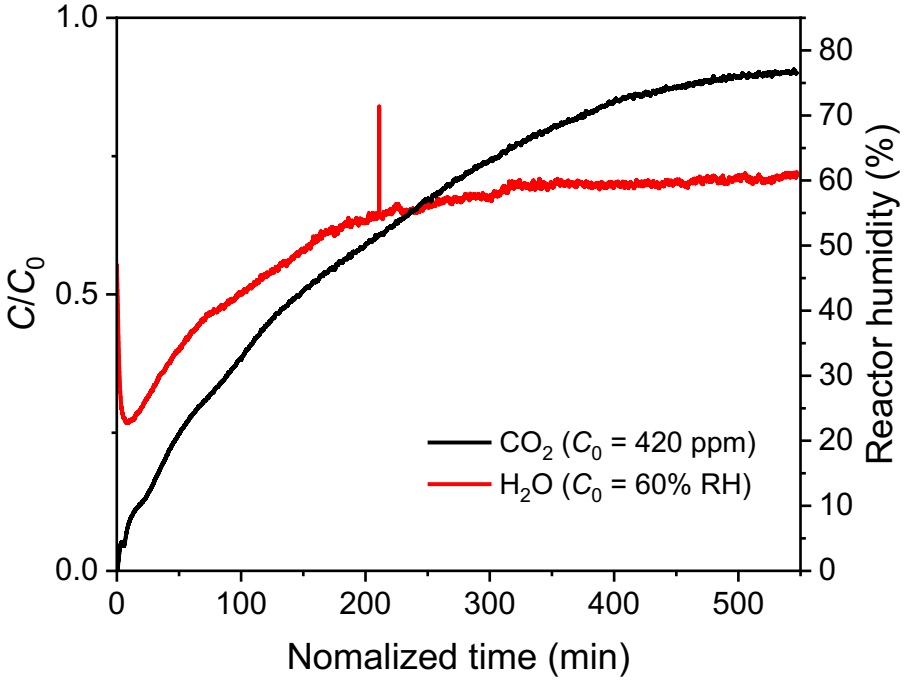

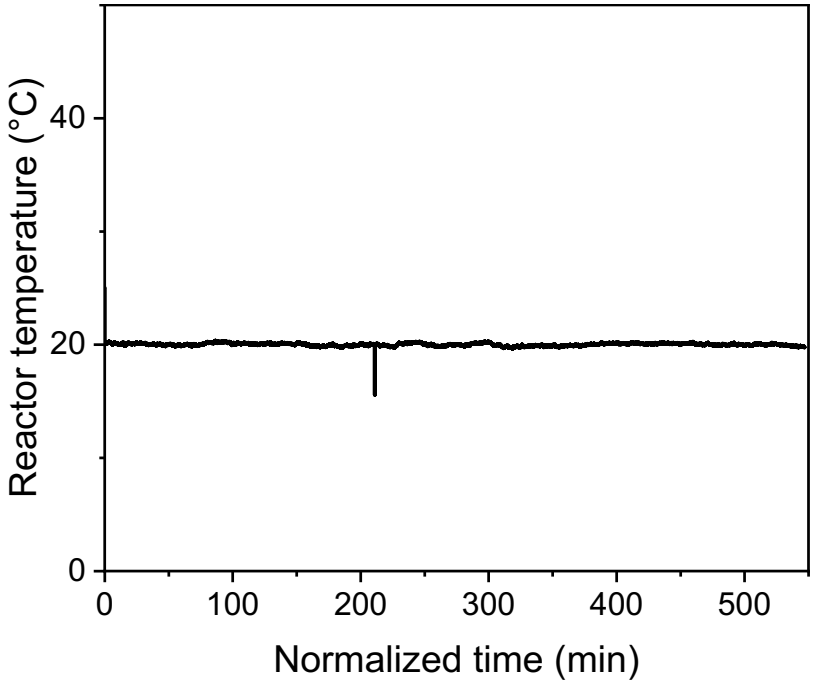

Supplementary Fig. 17 | Dynamic breakthrough measurements of KOH-WPI AF microbead using compressed air at 20 °C. 100 ± 10 mg of microbeads were degassed at 90 °C for 30 min in N_2, cooled down by methanol, and then prehumidified for 10 min before exposure to air.

Section 11. Single-Component Nitrogen Sorption Measurements

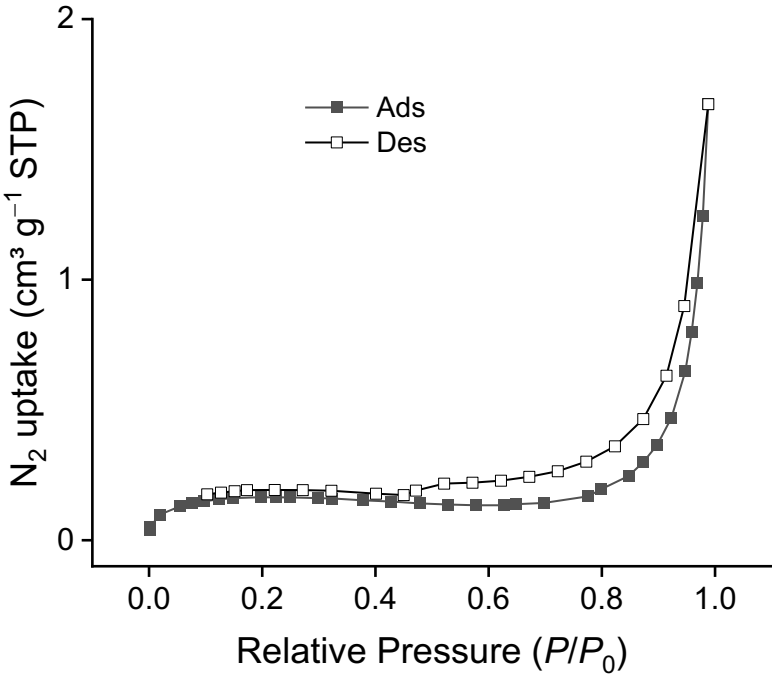

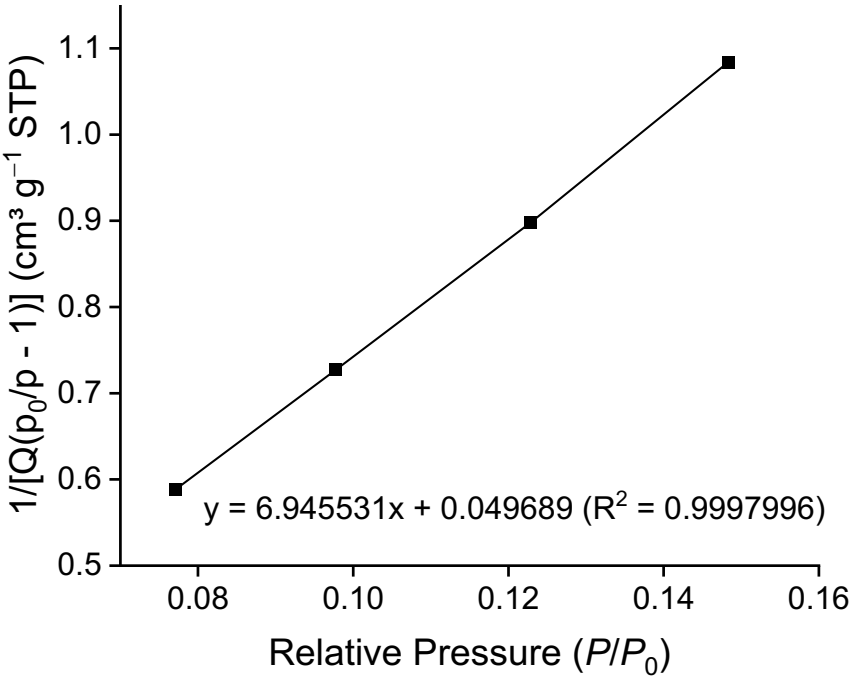

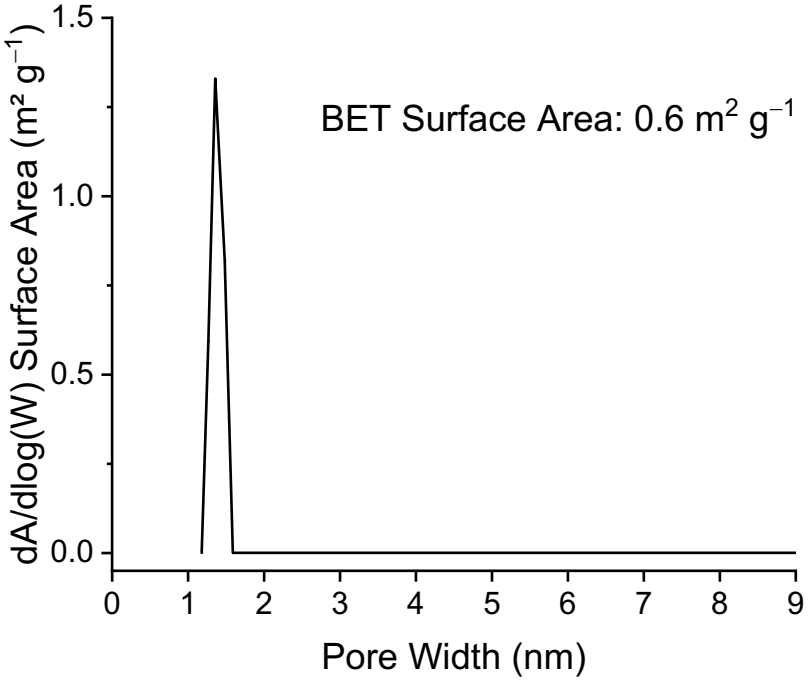

Supplementary Fig. 18 | N_2 sorption isotherms of KOH-*β*-lg AF microbeads measured at 77 K, corresponding BET plot, linear fitting, and pore size distribution calculated from the sorption isotherm. P is nitrogen pressure; P_0 = 1 atm under standard temperature and pressure. The BET surface area of the microbead is 0.6 m^2 g^{-1}.

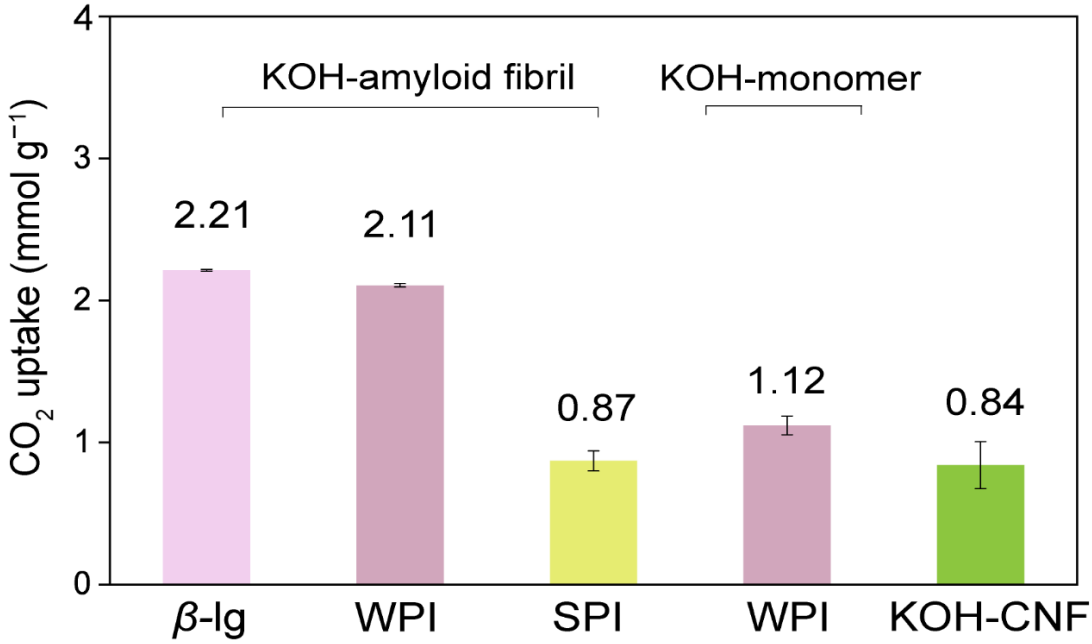

Supplementary Fig. 19 | CO_2 uptake of KOH-modified AF (*β*-lg, WPI, and SPI), WPI monomer, and CNF microbeads under humid simulated air. The data shown are statistical averages, and the error bars represent 1 standard deviation.

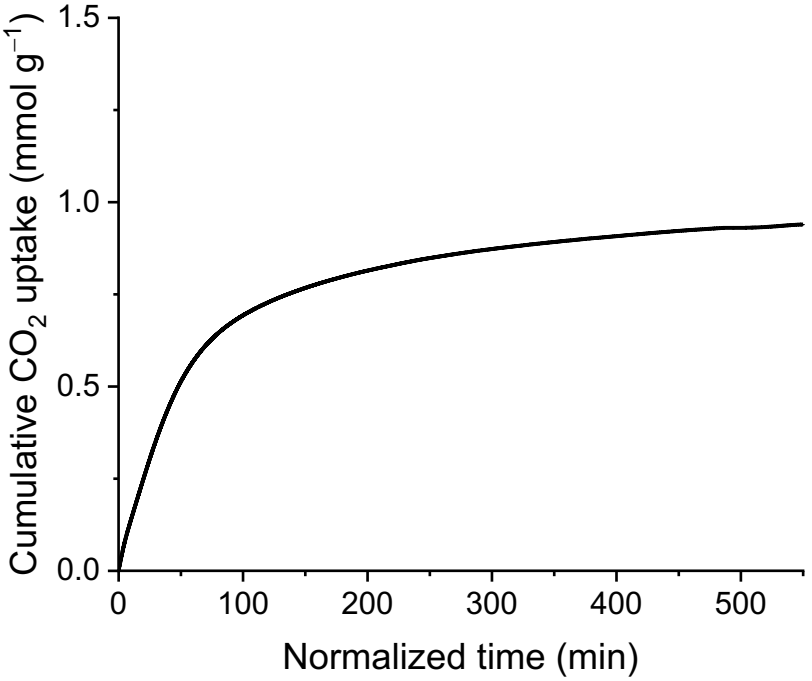

Supplementary Fig. 20 | Cumulative CO_2 uptake of the KOH-SPI AF microbead using simulated air (500 ppm of CO_2 balanced in N_2 with 50% RH) at 20 °C. The specific CO_2 uptake of the sample was then obtained as the difference between the observed CO_2 concentration and the expected value. The final CO_2 uptake shown in this figure was 0.93 mmol g^{-1}.

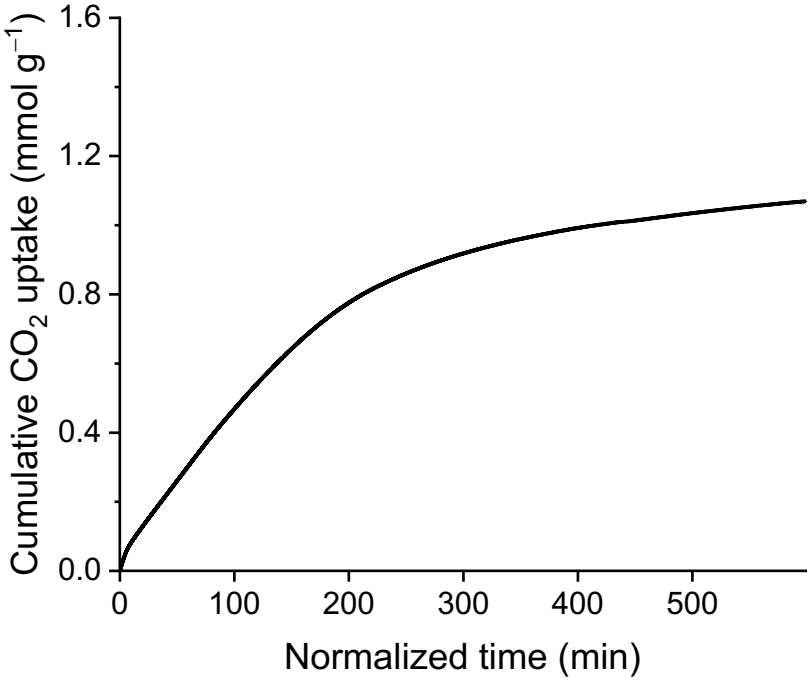

Supplementary Fig. 21 | Cumulative CO_2 uptake of the KOH-WPI monomer microbead using simulated air (500 ppm of CO_2 balanced in N_2 with 50% RH) at 20 °C. The specific CO_2 uptake of the sample was then obtained as the difference between the observed CO_2 concentration and the expected value. The final CO_2 uptake shown in this figure was 1.06 mmol g^{-1}.

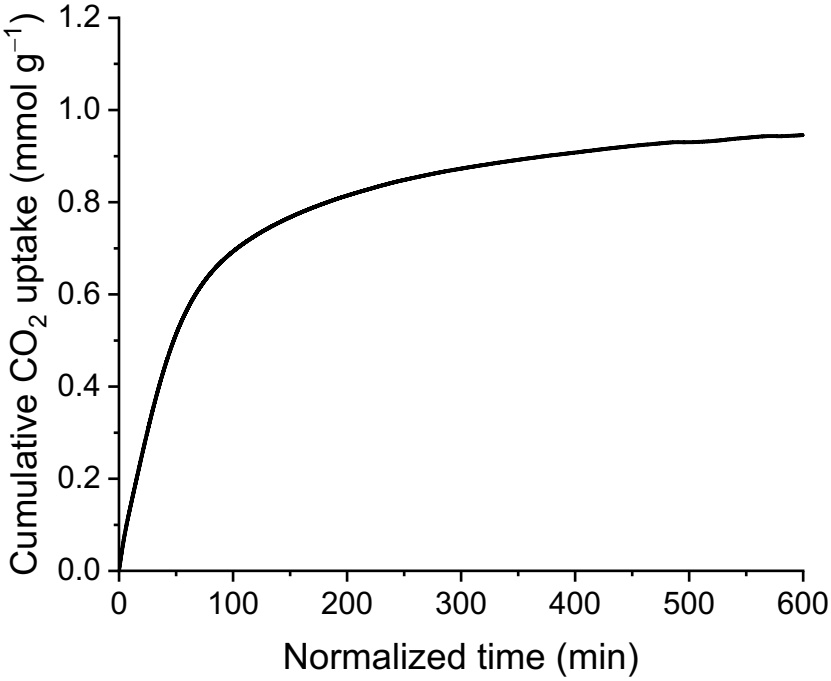

Supplementary Fig. 22 | Cumulative CO_2 uptake of the KOH-CNF microbead using simulated air (500 ppm of CO_2 balanced in N_2 with 50% RH) at 20 °C. The specific CO_2 uptake of the sample was then obtained as the difference between the observed CO_2 concentration and the expected value. The final CO_2 uptake shown in this figure was 0.95 mmol g^{-1}.

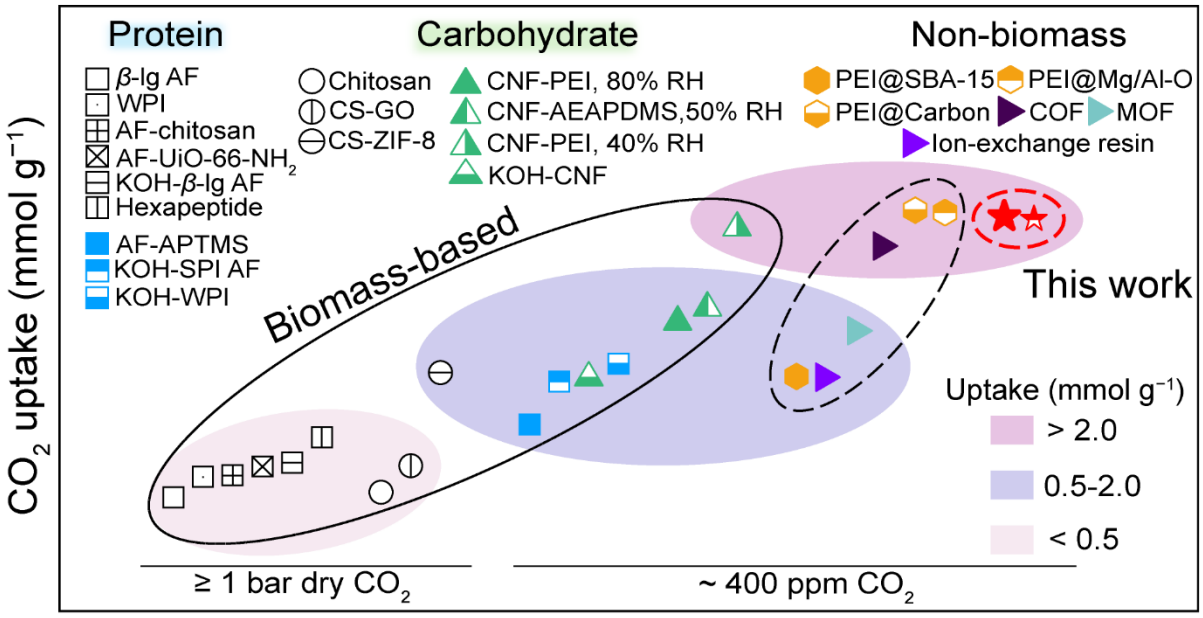

Supplementary Fig. 23 | CO_2 adsorption uptake comparison of selected bio- and non-bio-based sorbents for concentrated (~1 bar CO_2) and atmospheric CO_2 capture (Supplementary Tables 3–6).

Section 12. Detailed Sorbent Comparison for Direct Air Capture

Supplementary Table 3 | Adsorption, desorption, and cycling properties of selected sorbents for DAC using ambient air or simulated air.

Sorbent	CO_2 uptake (mmol g^{-1})	Adsorption conditions				Desorption condition	Cycling Stability	Ref.
		CO_2	Temp. (°C)	RH (%)	Carrier gas			
Ambient air								
HIPE templated p(NMe_3^+-MS OH^-)	0.49	Open air	18	20	-	95% RH	1 cycle	3
Pickering polyHIPEs	0.72	Open air	18	20	-	95% RH	1 cycle	4
Amine-based resin	1.11	Open air	25	35–60	-	100 °C Water vapor	9 cycles	5
COF-999	1.28	Open air	-	-	-	60 °C	100 cycles	6
Simulated air								
Charged sorbent PCS-OH	0.2	400 ppm	30	0	N_2/O_2	130 °C	10 cycles, stable	7
CO_3^{2-}-resin	0.26	417 ppm	20	0	N_2/O_2	95% RH	5 cycles, stable	8
MOF-808-Lys	0.70	400	25	50	N_2/O_2	140 °C	10 cycles, stable	9
Amine-based anion exchange polypropylene	0.98	400	23	0.5	N_2/O_2	water	1 cycle	10
MOF-74-mmen-2	1.05	390	25	0	N_2/O_2	150 °C	10 cycles, stable	11
$Zn(ZnOH)_4(bibta)_3$	1.32	395	25	0	N_2/O_2	100 °C	5 cycles, stable	12

Supplementary Table 4 | Adsorption, desorption, and cycling properties of selected protein-based DAC sorbents.

Sorbent	CO_2 uptake (mmol g^{-1})	Adsorption conditions				Desorption condition	Cycling Stability	Ref.
		CO_2	Temp. (°C)	RH (%)	Carrier gas			
Protein monomer[a]								
Commercial Whey protein isolate	0.091	1bar	30	0		N_2,30 °C	15 cycles, 20% loss	13
Spray-dried Whey protein isolate (130 °C)	0.177	1bar	30	0		N_2,30 °C	15 cycles, 20% loss	
Spray-dried Whey protein isolate (170 °C)	0.168	1bar	30	0		N_2,30 °C	15 cycles, 20% loss	
Protein amyloid fibril[b]								
Natural hexapeptide VQIVYK	0.48	1bar	37	100%	N_2	N_2,100°C	3 cycles, stable	14
Synthesized Hexapeptide VQIVYKK	0.54	1ba	37	100%	N_2	N_2,100°C	3 cycles, stable	
Synthesized Hexapeptide VKIVYK	0.74	1ba	37	100%	N_2	N_2,100°C	3 cycles, stable	
APTMS-modified β-lg aerogel (1:1)	0.73	1bar	25	0	N_2	N_2,150°C	3 cycles, stable	15
diAPTMS-modified β-lg aerogel (1:1)	0.85	1bar	25	0	N_2	N_2,150°C	3 cycles, stable	
triAPTMS-modified β-lg aerogel (1:1)	0.92	1bar	25	0	N_2	N_2,150°C	3 cycles, stable	
triAPTMS-modified β-lg aerogel (1:4)	1.02	1bar	25	0	N_2	N_2,150°C	3 cycles, stable	
triAPTMS-modified lysozyme aerogel (1:4)	0.3	1bar	25	0	N_2	N_2,150°C	3 cycles, stable	
triAPTMS-modified black bean aerogel (1:4)	0.41	1bar	25	0	N_2	N_2,150°C	3 cycles, stable	
Low MW chitosan-BLG aerogel	0.16	1bar	25	0	N_2	N_2,150°C	3 cycles, stable	
medium MW chitosan-aerogel	0.18	1bar	25	0	N_2	N_2,150°C	3 cycles, stable	
high MW chitosan-aerogel	0.41	1bar	25	0	N_2	N_2,150°C	3 cycles, stable	
30% UiO-66-NH_2 hybrid	0.11	1bar	25	0	N_2	N_2,150°C	3 cycles, stable	16
40% UiO-66-NH_2 hybrid	0.16	1bar	25	0	N_2	N_2,150°C	3 cycles, stable	
50% UiO-66-NH_2 hybrid	0.25	1bar	25	0	N_2	N_2,150°C	3 cycles, stable	

a, Calculated from the weight increase (%) as mmol g^{-1} monomer.

b, Breakthrough experiments and single-component isotherm results.

Supplementary Table 5 | Adsorption, desorption, and cycling properties of selected carbohydrate-based DAC sorbents.

Sorbent	CO_2 uptake (mmol g^{-1})	Adsorption conditions				Desorption condition	Cycling Stability	Ref.
		CO_2	Temp. (°C)	RH (%)	Carrier gas			
Carbohydrate								
CTS/ZIF-8 composite	0.99	1 bar	30	0	-	vacuum, 90 °C	10 cycles, 4.35% loss	3
Pure chitosan	0.05	5 bar	25	0	-	-	-	4
Chitosan Grafted Graphene Oxide Aerogel	0.26	1 bar	25	-	-	-	-	6
AEAPDMS-NFC-FD	1.39	506 ppm	25	40	Compressed air	Ar, 90 °C	20 cycles, 50% loss	17,18
Nanofibrillated Cellulose-Polyethylenimine Foams (PEI-44)	1.55	400 ppm	25	40	Ambient air	N_2, 85°C	5 cycles, 3% loss	19
	~2.13[a]	400 ppm		80	-	-	-	

a, estimated from the CO_2 uptake curve versus humidity.

Supplementary Table 6 | Adsorption, desorption, and cycling properties of selected non-biomass-based DAC sorbents.

Sorbent	CO_2 uptake (mmol g^{-1})	Adsorption conditions				Desorption condition	Cycling Stability	Ref.
		CO_2	Temp. (°C)	RH (%)	Carrier gas			
Amine-functionalized porous support								
PEI@SBA-15	0.96	400 ppm	35	0	He	110 °C	20 cycles, stable	20
PEI@Mesoporous carbon	2.25	400 ppm	25	0	N_2	110 °C	20 cycles, stable	21
PEI@Mg0.55Al-O	2.27	400 ppm	25	0	N_2	120 °C	20 cycles, 14% loss	22
Covalent/Metal Organic Framework								
$Zn(ZnOH)_4(bibta)_3$	1.32	395 ppm	25	0	N_2/O_2	100 °C	5 cycles, stable	12
COF-999	2.02	400 ppm	25	50	N_2/O_2	60 °C	100 cycles, stable	23
Ion-exchange resin								
Amine-based anion exchange resin in polypropylene	0.98	400 ppm	23	0.5	N_2/O_2	water	1 cycle	10

Section 13. Instrument for Desorption and Regeneration

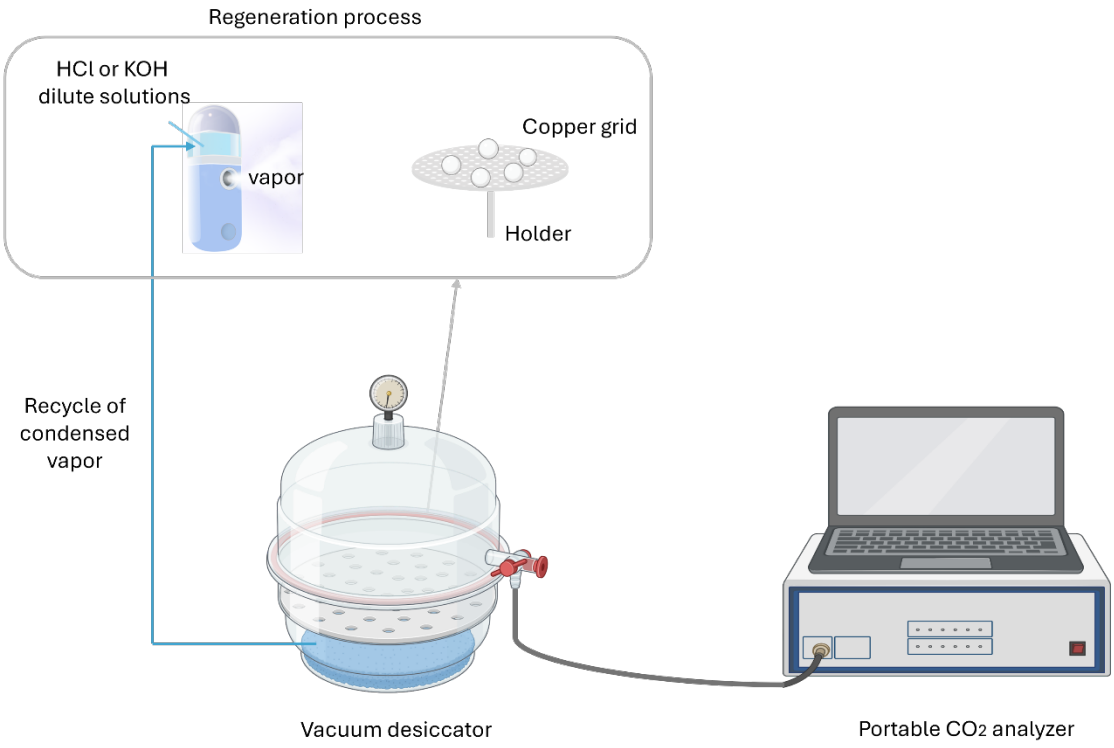

Supplementary Fig. 24 | Schematic diagram of the desorption and regeneration instrument. 10 ml of acid/alkaline solution was loaded into the automatic humidifier (30 ml, 3 W, 5 V) with an acidic/alkaline mist production rate of 1.25–1.45 ml/min. The CO_2 in the 9.3 L reactor (vacuum desiccator) was removed by purging pure N_2 for 30 min. After the N_2 purging was ceased, the mist was generated for 13–15 min. The condensation of the mist was facilitated by an ice bath around the bottom of the desiccator.

Section 14. Dynamic Desorption and Regeneration Measurements

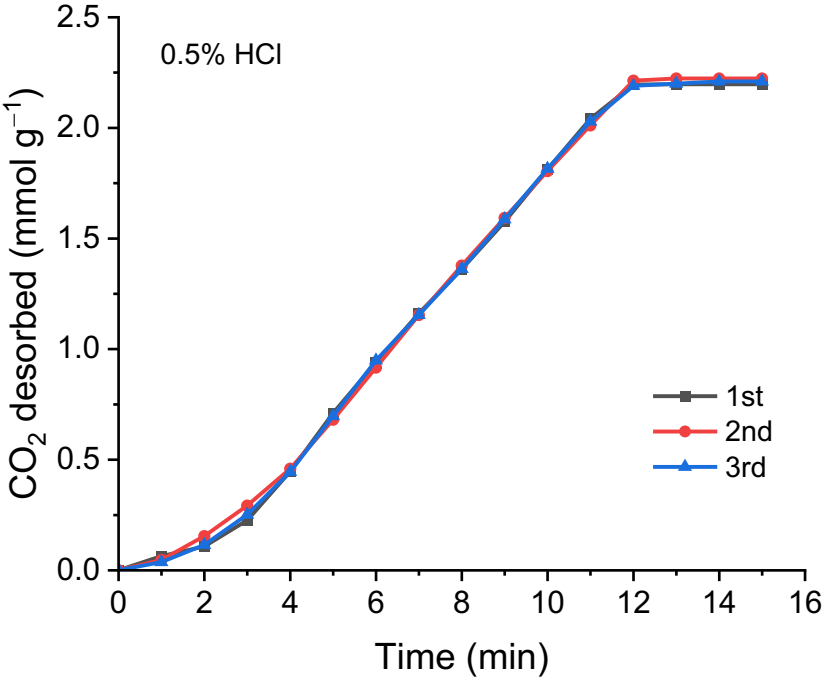

Supplementary Fig. 25 | Dynamic desorption curves of saturated KOH-WPI AF microbeads under ambient air (~420 ppm CO_2, 40–60% relative humidity, 25 °C) using 0.5% HCl solutions. The gas inside the reactor was removed by N_2 purge for 30 min. The experiment was repeated three times.

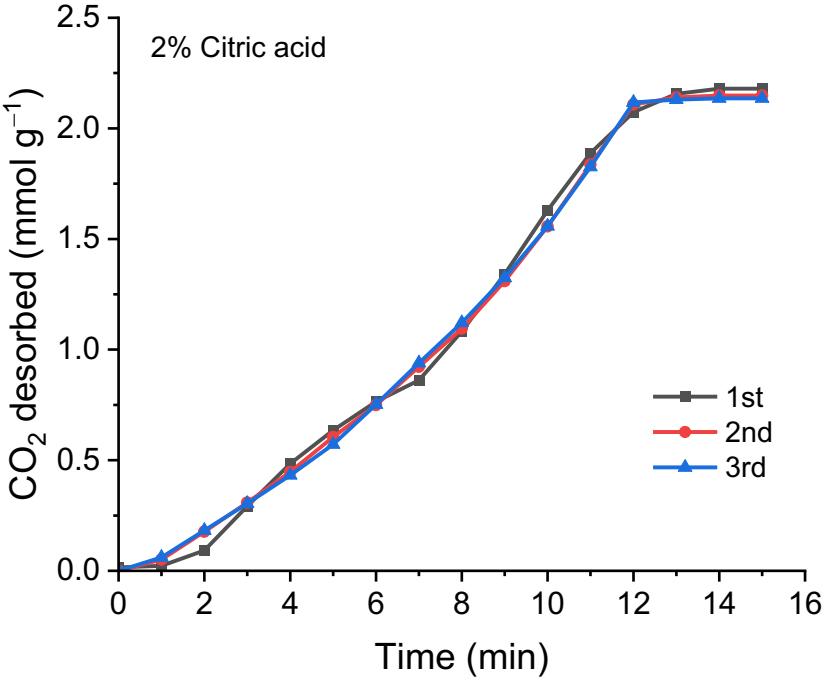

Supplementary Fig. 26 | Dynamic desorption curves of saturated KOH-WPI AF microbeads under ambient air (~420 ppm CO_2, 40–60% relative humidity, 25 °C) using 2% citric acid solutions. The gas inside the reactor was removed by N_2 purge for 30 min. The experiment was repeated three times.

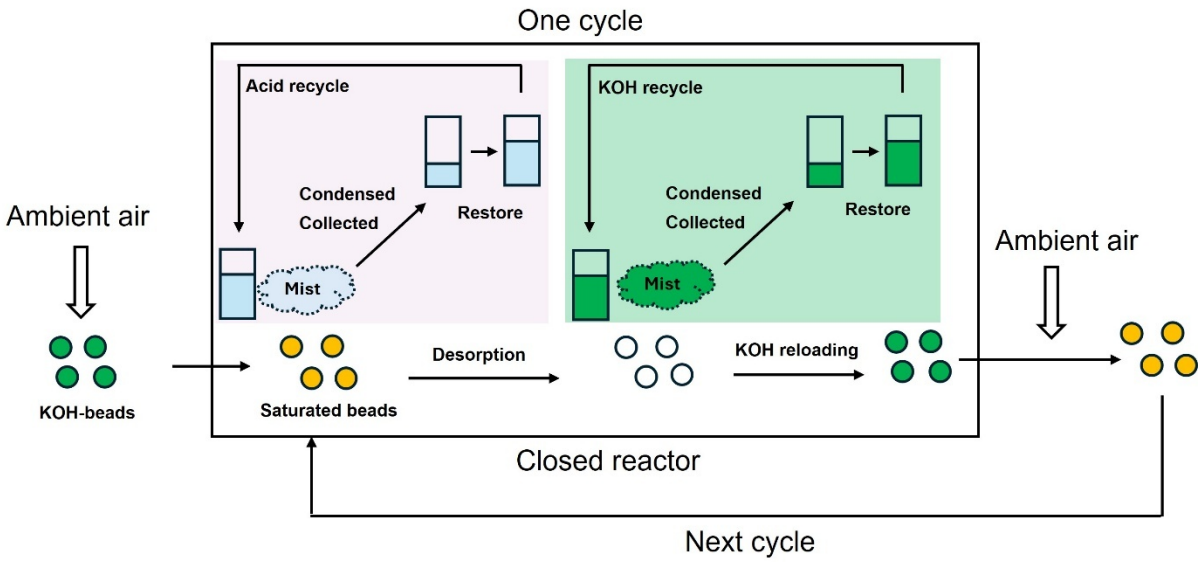

Supplementary Fig. 27 | A schematic of the acid-alkali mist regeneration cycle. KOH-WPI AF microbeads were saturated by ambient air (~420 ppm CO_2, 40–60% relative humidity, 25 °C) for 12–14 h. The acid or alkaline mist was collected by condensation and then restored to the initial value by adding fresh solutions in the humidifier. The desorption and regeneration process is continuous without any sample drying.

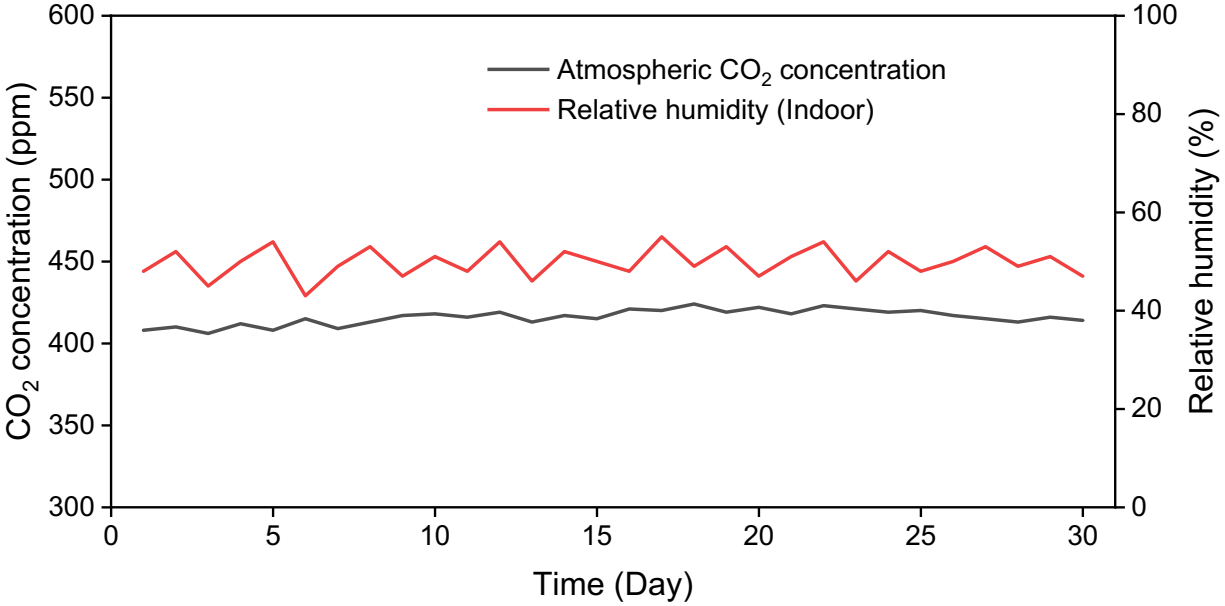

Supplementary Fig. 28 | Atmospheric CO_2 concentration (black) and RH (red) for 30 continuous days of operation using ambient air in Zürich, Switzerland.

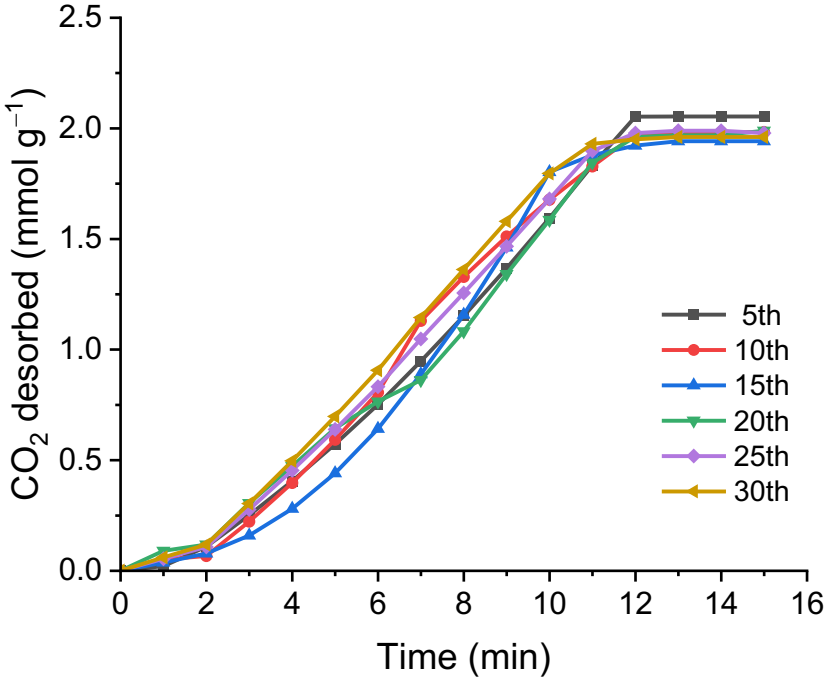

Supplementary Fig. 29 | Dynamic desorption curves of KOH-WPI AF microbeads saturated by ambient air (~420 ppm CO_2, 40–60% relative humidity, 25 °C) after 5th, 10th, 15th, 20th, 25th, and 30th regeneration using 0.5% HCl solutions.

Supplementary Table 7 | The mist consumption of 0.5% HCl and 0.5% KOH during 30 cycles. The condensed HCl or KOH mist was collected and weighed, and the consumption was calculated from the difference in weight from the initial value (~10 g) for each cycle. The density of 0.5% HCl and 0.5 % KOH at room temperature was assumed to be 1.002 g ml^{-1} and 1.005 g ml^{-1}, respectively.

Cycle	HCl solution final weight (g)	HCl solution consumption (g)	KOH solution final weight (g)	KOH solution consumption (g)
0	10.071		10.050	
1	8.168	1.903	8.193	1.857
2	8.084	1.987	8.969	1.081
3	8.452	1.619	8.745	1.305
4	8.355	1.716	8.452	1.598
5	8.095	1.976	8.496	1.554
6	8.258	1.813	8.78	1.27
7	8.37	1.701	8.039	2.011
8	8.417	1.654	8.6	1.45
9	8.382	1.689	8.6	1.45
10	8.256	1.815	8.935	1.115
11	8.096	1.975	8.079	1.971
12	8.126	1.945	8.501	1.549
13	8.468	1.603	8.895	1.155
14	8.165	1.906	8.857	1.193
15	8.262	1.809	8.422	1.628
16	8.234	1.837	9.011	1.039
17	8.2	1.871	8.684	1.366
18	8.481	1.59	8.708	1.342
19	8.348	1.723	8.69	1.36
20	8.462	1.609	8.553	1.497
21	8.355	1.716	8.398	1.652
22	8.431	1.64	8.934	1.116
23	8.361	1.71	8.829	1.221
24	8.1	1.971	9.006	1.044
25	8.01	2.061	8.041	2.009
26	8.468	1.603	8.226	1.824
27	8.181	1.89	8.76	1.29
28	8.456	1.615	8.115	1.935
29	8.232	1.839	8.557	1.493
30	8.462	1.609	8.432	1.618

Section 15. Thermogravimetric Analysis (TGA)

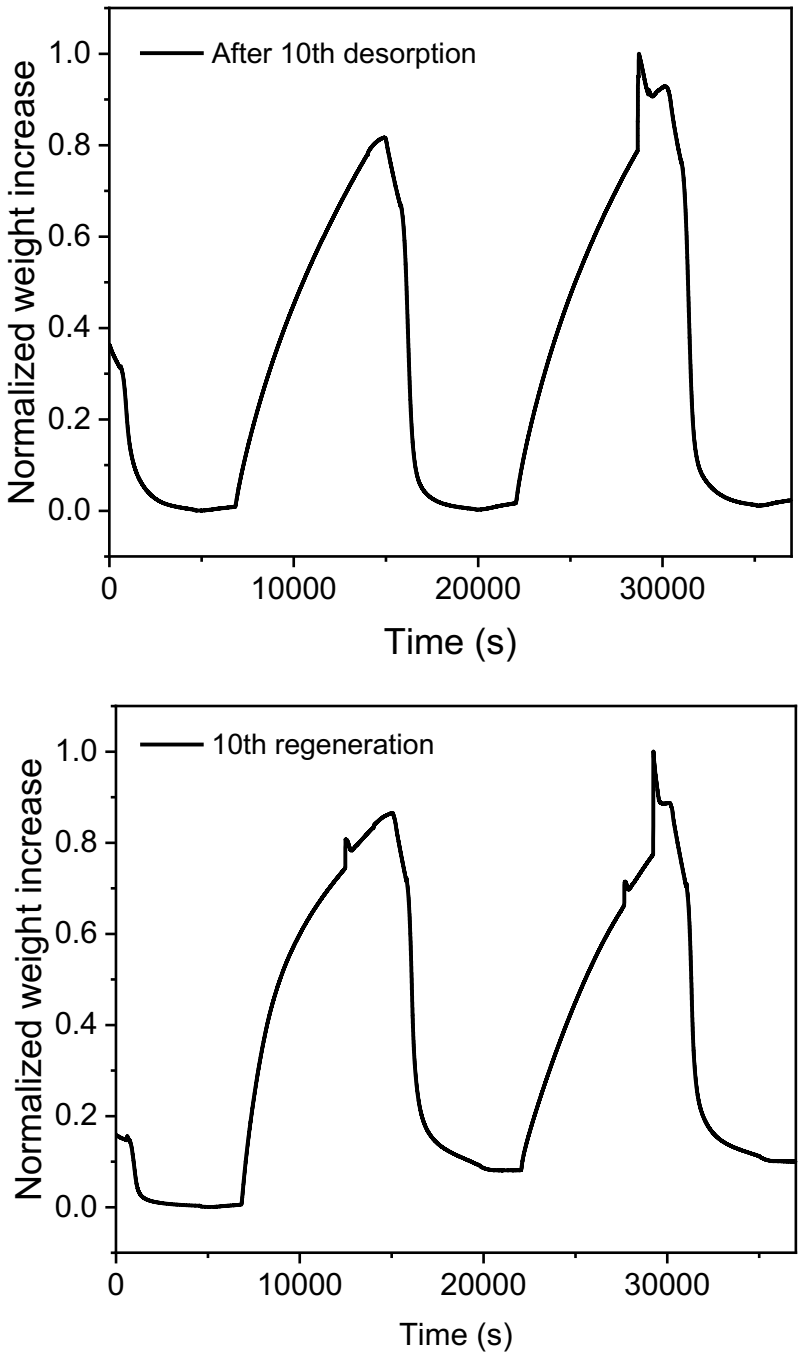

Supplementary Fig. 30 | TGA curves of desorbed and regenerated KOH-WPI AF microbeads (10th) using compressed air (~420 ppm of CO_2, ~21% O_2, balanced in N_2) with 55% RH at 20 °C. Before the actual CO_2 adsorption measurements, the samples were degassed at 150 °C in N_2 for 30 min. CO_2 was then desorbed by pure N_2, heated to 120 °C at a rate of 10 °C per min, and held at this temperature for 30 min.

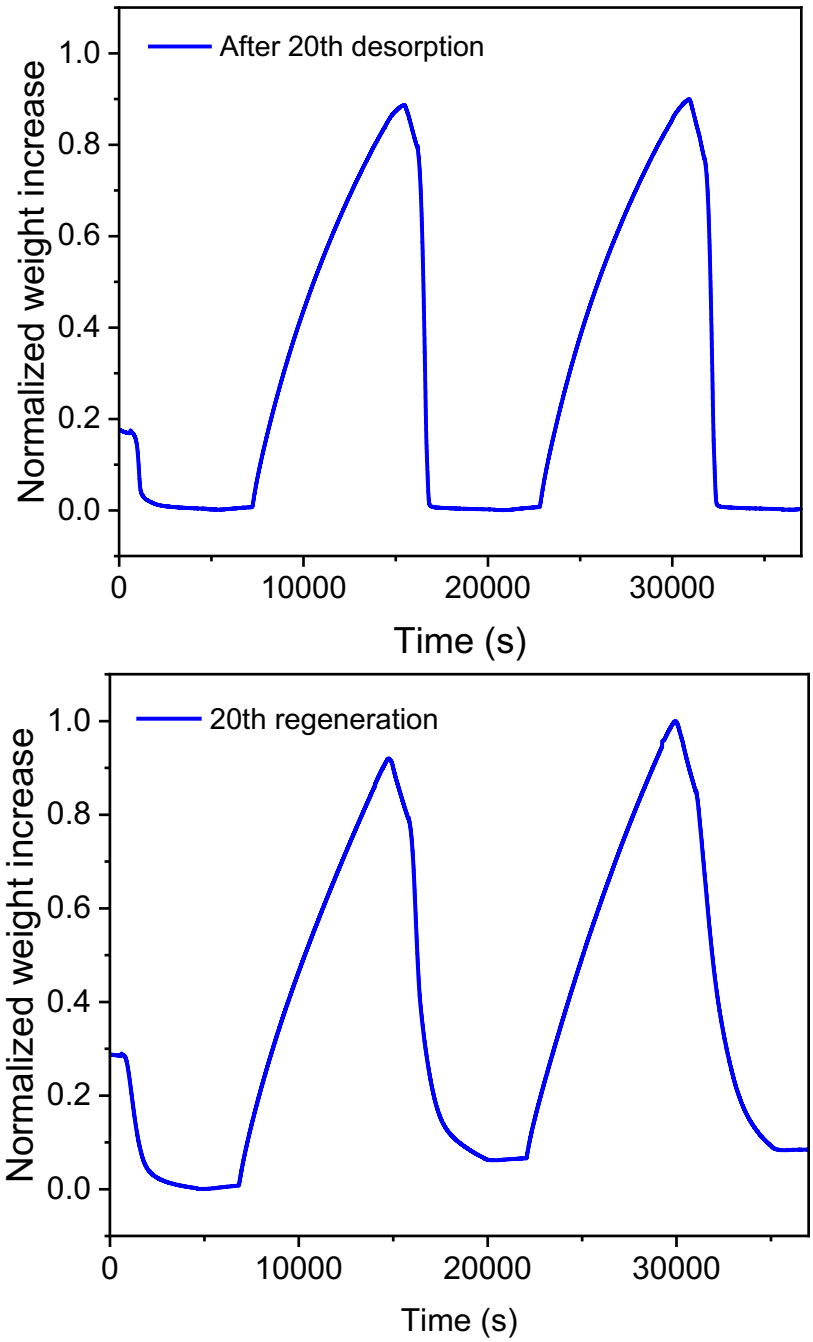

Supplementary Fig. 31 | TGA curves of desorbed and regenerated KOH-WPI AF microbeads (20th) using compressed air (~420 ppm of CO_2, ~21% O_2, balanced in N_2) with 55% RH at 20 °C. Before the actual CO_2 adsorption measurements, the samples were degassed at 150 °C in N_2 for 30 min. CO_2 was then desorbed using pure N_2, heated to 120 °C at a rate of 10 °C per min, and held at this temperature for 30 min.

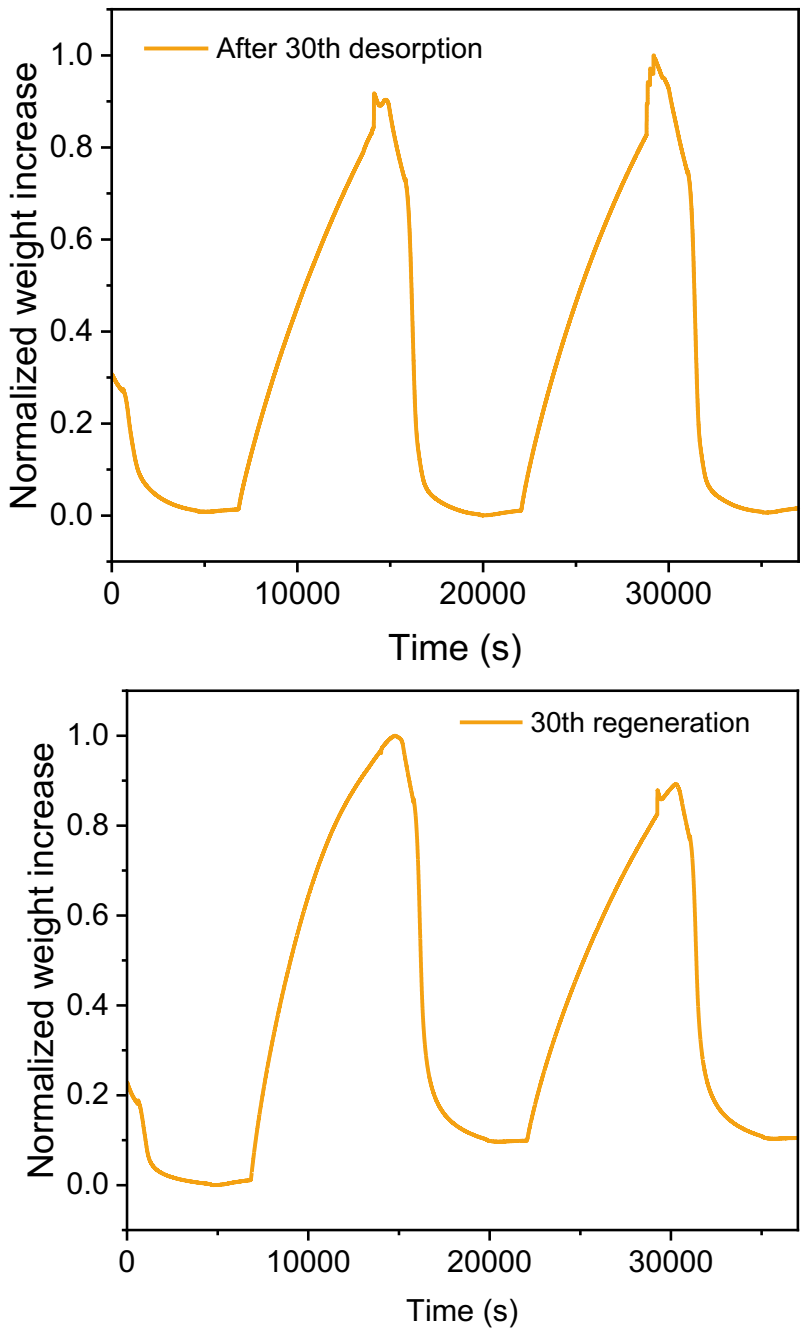

Supplementary Fig. 32 | TGA curves of desorbed and regenerated KOH-WPI AF microbeads (30th) using compressed air (~420 ppm of CO_2, ~21% O_2, balanced in N_2) with 55% RH at 20 °C. Before the actual CO_2 adsorption measurements, the samples were degassed at 150 °C in N_2 for 30 min. CO_2 was then desorbed by pure N_2, heated to 120 °C at a rate of 10 °C per min, and held at this temperature for 30 min.

Section 16. Density Functional Theory (DFT) Calculations

Carbamate pathway

Supplementary Table 8 | Reaction 1. ε-amino group of a single Lys residue (Lys-NH_2) attacks the CO_2 molecule, forms a transition state-1 (TS-1), and finally becomes intermediate-1 (Int-1): Lys-$NH_2^+COO^-$.

Name	Pathway	Delta G (kJ mol^{-1})
Initial state	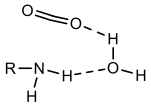	0
Transition state-1	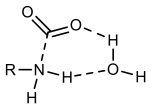	24.9
Intermediate-1	R—$NH_2^+COO^-$ + H_2O	−31.2

Supplementary Table 9 | Reaction 1-1. Int-1 undergoes proton rearrangement through the hydrogen bond with water, forms another transition state (TS-1-1), and finally becomes Lys-RNHCOOH.

Name	Pathway	Delta G (kJ mol^{-1})
Intermediate-1	R—$NH_2^+COO^-$ + H_2O	0
Transition state-1-1	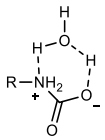	43.6
Product	R—NHCOOH + H_2O	−68.9

Supplementary Table 10 | Reaction 2. Proton transfer occurs between the Int-1 and the hydroxide ion, which is a barrier-free reaction (strong base to weak base).

Name	Pathway	Delta G (kJ mol^{-1})
Initial state	R—$NH_2^+COO^-$ + OH^-	0
Product	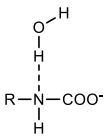	−133.9

Supplementary Table 11 | Reaction 3. Proton transfer occurs between the Int-1 and the carbonate (stronger base than ε-amino group).

Name	Pathway	Delta G (kJ mol^{-1})
Initial state	R—$NH_2^+COO^-$ + CO_3^{2-}	0
Product	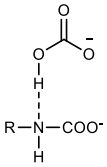	−103.0

Bicarbonate pathway

Supplementary Table 12 | Reaction 4. The ΔG value is positive, indicating that the reaction is non-spontaneous and requires external energy, and is not driven by entropy alone.

Name	Pathway	Delta G (kJ mol^{-1})
Initial state	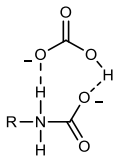	0
Transition state	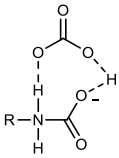	−10.4
Product	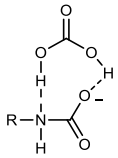	7.4

Supplementary Table 13 | Reaction 5. The ε-amino group acts as a hydrogen acceptor, catalyzing the reaction between hydroxide ion and CO_2 to form a hydrogen-bonded bicarbonate complex.

Name	Pathway	Delta G (kJ mol^{-1})
Initial state	$R{-}NH_2 + OH^- + CO_2$	0
Product	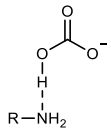	−160.3

Supplementary Table 14 | Reaction 6. Water transfers a proton to the ε-amino group, resulting in a hydroxide ion, which subsequently attacks the CO_2, forming transition state 3 (TS-3). The final product is the bicarbonate-ammonium complex.

Name	Pathway	Delta G (kJ mol^{-1})
Initial state	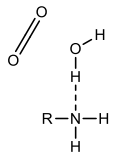	0
Transition state	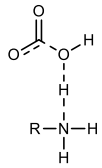	41.3
Product	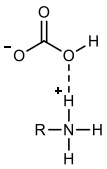	−72.8

Supplementary Table 15 | Reaction 7. Ammonium ions form hydrogen bond complexes with water, which prevent water from reacting with CO_2.

Name	Pathway	Delta G (kJ mol^{-1})
Initial state	$R{-}NH_2$ + OH^- + CO_2	0
Product	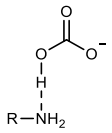	−19.5

Supplementary Table 16 | Reaction 8. Hydroxide ion attacks the CO_2 to form bicarbonate.

Name	Pathway	Delta G (kJ mol^{-1})
Initial state	OH^- + CO_2	0
Product	HCO_3^-	−127.2

Supplementary Table 17 | Reaction 9. Carbonate reacts with CO_2 and water to form bicarbonate.

Name	Pathway	Delta G (kJ mol^{-1})
Initial state	$CO_2 + CO_3^{2-} + H_2O$	0
Product	HCO_3^-	−75.35

Supplementary Table 18 | Reaction 10. The dicarbonate and ammonium ions undergo proton transfer, and the dicarbonate decomposes to produce bicarbonate and carbon dioxide.

Name	Pathway	Delta G (kJ mol^{-1})
Initial state	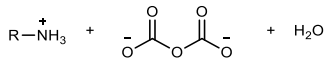	0
Product	$R{-}NH_2 + CO_2 + HCO_3^- + H_2O$	23.9

Geometric constraints on the carbamate pathway

Supplementary Table 19 | Reaction 11. Due to the fixed 4–5 Å spacing between two Lys ε-amino groups within the fibril stack, water acts as a bridge for proton transfer, forming transition state-4 (TS-4) and finally becomes intermediate-4 (Int-4). Protons from Int-4 transfer preferentially to hydroxide, bicarbonate, or carbonate rather than to adjacent Lys residues.

Name	Pathway	Delta G (kJ/mol)
Initial state	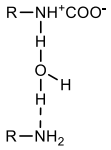	0
Transition state	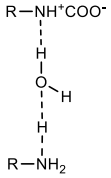	9.6
Product	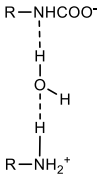	−35.4

Section 17. Single-Component CO_2 Sorption Measurements

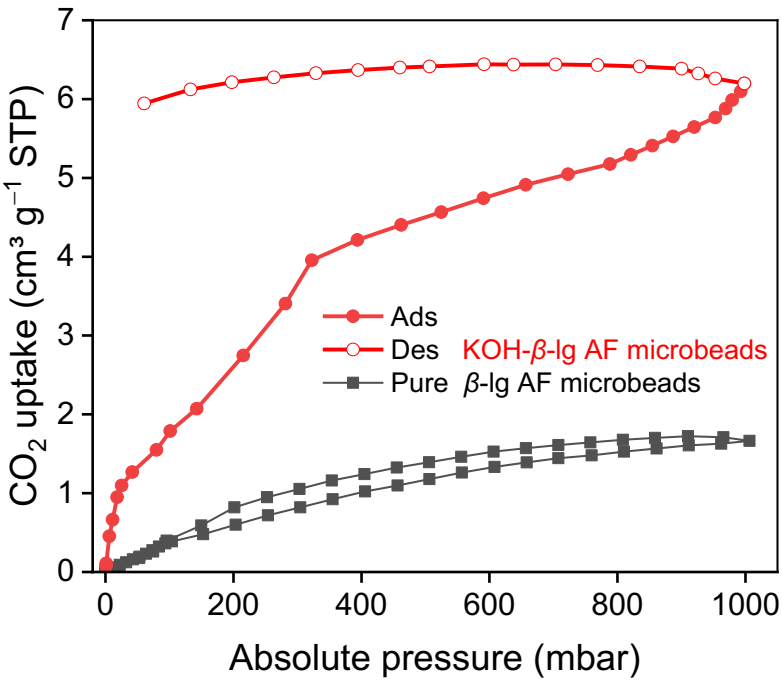

Supplementary Fig. 33 | Single-component CO_2 sorption isotherms of KOH-*β*-lg AF microbead measured at 298 K. Before the measurements, the samples were degassed by N_2 under vacuum for 5 h at 150 °C. The CO_2 capacity for pure (black curve) and KOH-modified (red curve) *β*-lg AF microbead is 0.08 mmol g^{-1} and 0.29 mmol g^{-1} at 1 bar, respectively.

Section 18. *In situ* Diffuse Reflectance Infrared Fourier Transform Spectroscopy (DRIFTS)

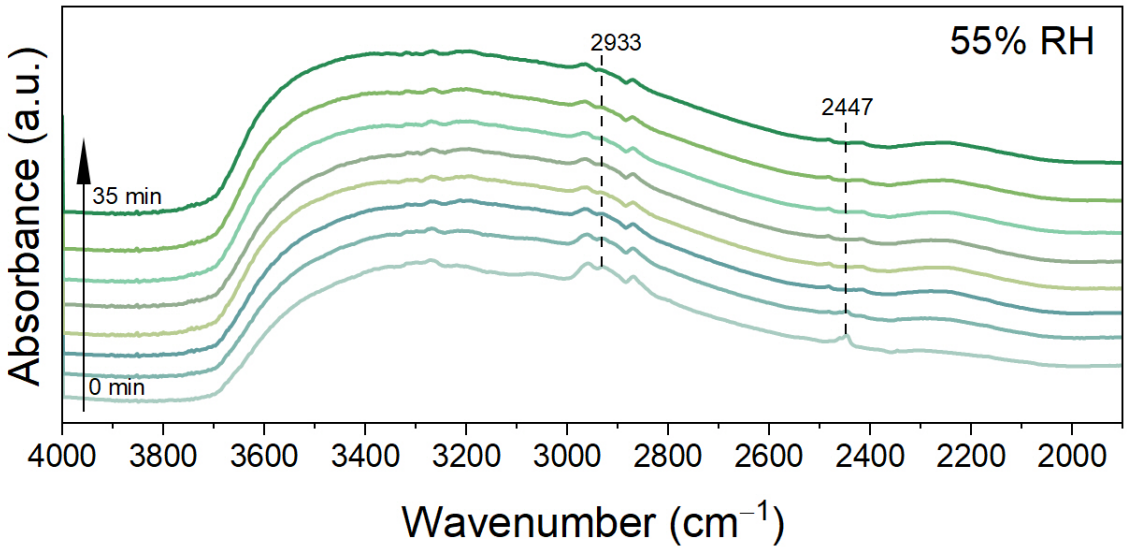

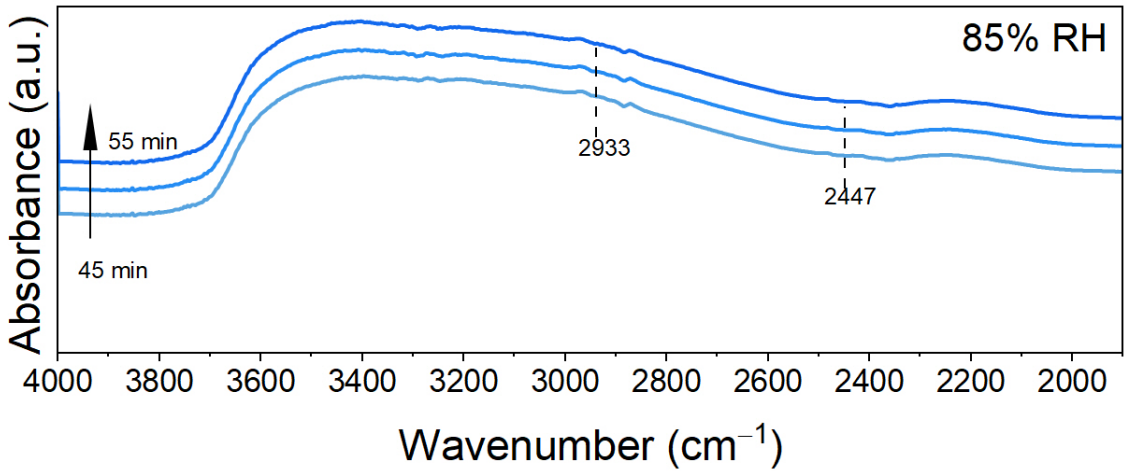

Supplementary Fig. 34 | Time-resolved *in situ* DRIFTS spectroscopy (4000 cm^{-1} to 1900 cm^{-1}) of KOH-*β*-lg AF microbead under compressed air (purified ambient air, ~420 ppm CO_2) at 25 °C with 55% RH (up) and 85% RH (down). The measurement interval for each spectrum is 5 min. Before the actual CO_2 adsorption measurements, the samples were degassed at 120 °C in N_2 for 30 min.

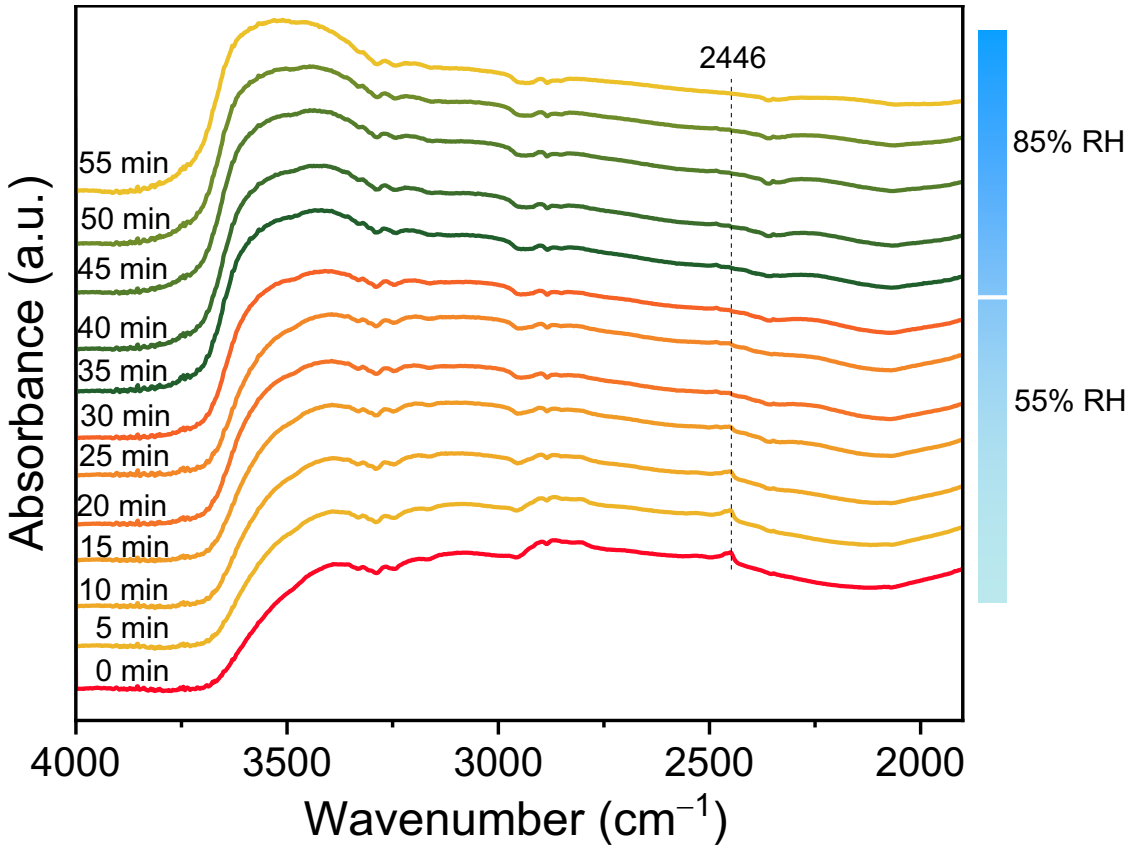

Supplementary Fig. 35 | Time-resolved *in situ* DRIFTS spectroscopy (4000 cm^{-1} to 1900 cm^{-1}) of KOH-CNF microbead under compressed air (purified ambient air, ~420 ppm of CO_2) at 25 °C under 55% RH and 85% RH. The measurement interval for each spectrum is 5 min. Before the actual CO_2 adsorption measurements, the samples were degassed at 120 °C in N_2 for 30 min.

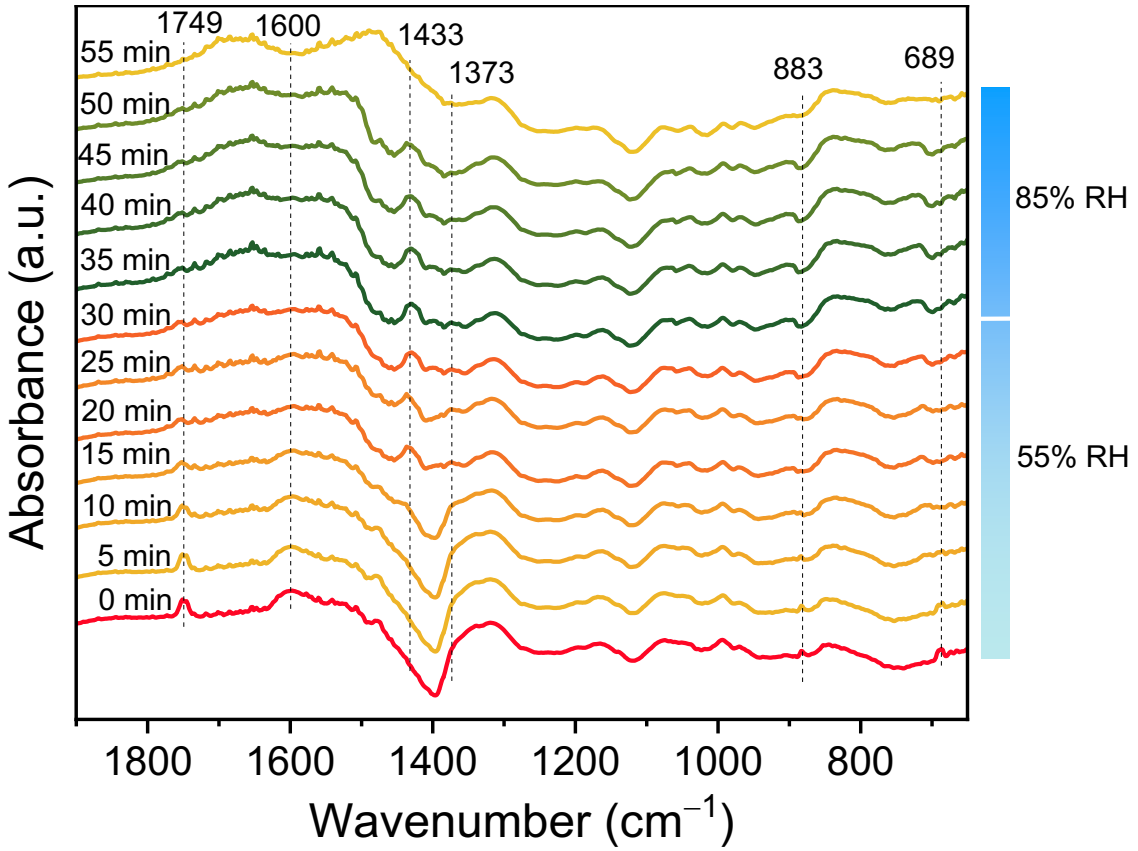

Supplementary Fig. 36 | Time-resolved *in situ* DRIFTS spectroscopy (1900 cm^{-1} to 650 cm^{-1}) of KOH-CNF microbead under compressed air (purified ambient air, ~420 ppm of CO_2) at 25 °C under 55% RH and 85% RH. The measurement interval for each spectrum is 5 min. Before the actual CO_2 adsorption measurements, the samples were degassed at 120 °C in N_2 for 30 min.

Section 19. Powder X-ray Diffraction (PXRD)

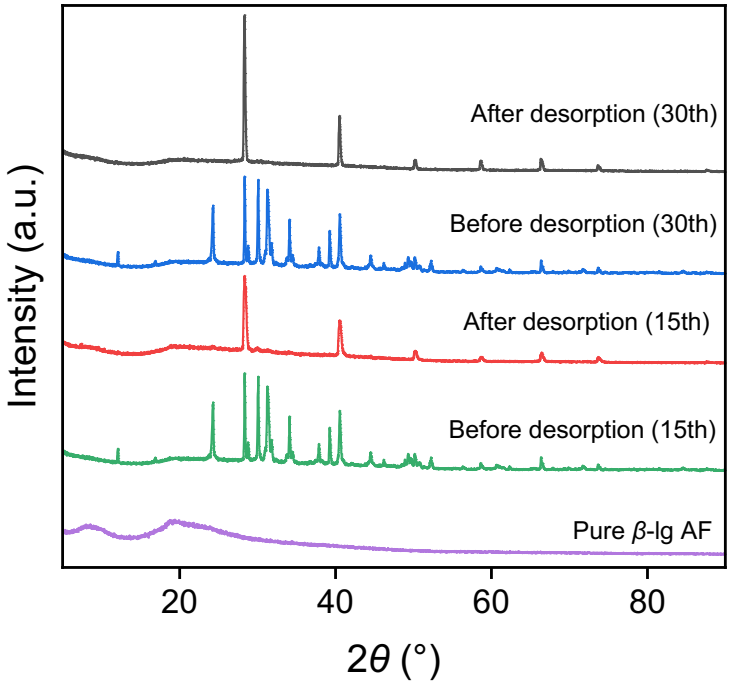

Supplementary Fig. 37 | PXRD patterns of KOH-WPI AF microbead after 15 and 30 cycles. The intensity values along the Y-axis were normalized for comparison.

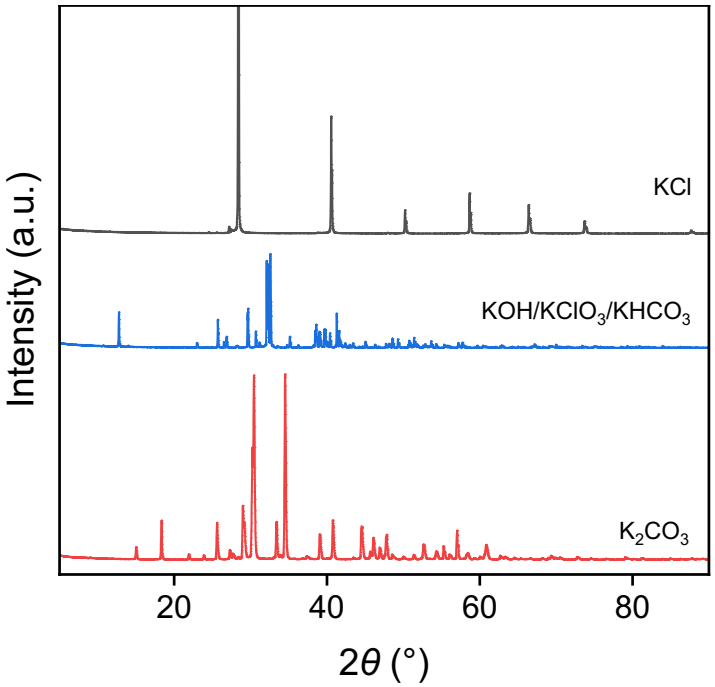

Supplementary Fig. 38 | PXRD patterns of the reference materials KCl, $KHCO_3$, and K_2CO_3. The intensity values along the Y-axis were normalized for comparison.

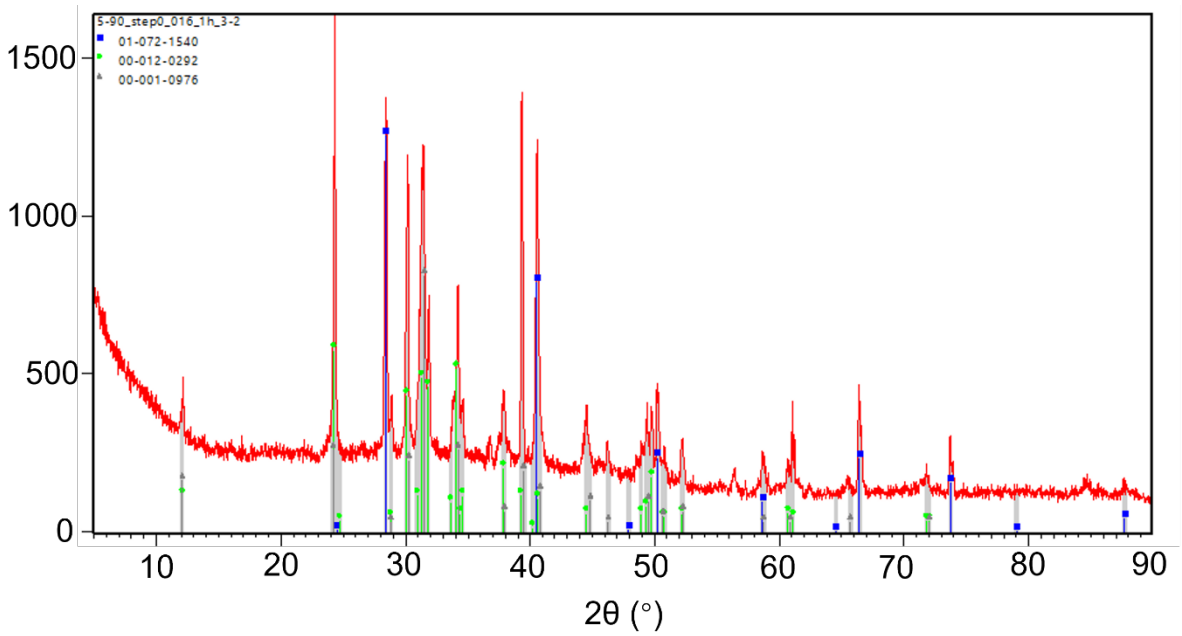

Visible	Ref. Code	Score	Compound Name	Displ. (°2θ)	Scale Fac.	Chem. Formula
1	01-072-1540	66	Potassium Chloride	0.000	0.765	KCl
2	00-012-0292	80	Potassium Hydrogen Carbonate	0.000	0.349	$KHCO_3$
3	00-001-0976	51	Potassium Hydrogen Carbonate	0.000	0.495	$KHCO_3$

Supplementary Fig. 39 and Supplementary Table 20 | PXRD pattern analysis of the KOH-WPI AF microbeads before desorption (15th) according to the ICSD database.

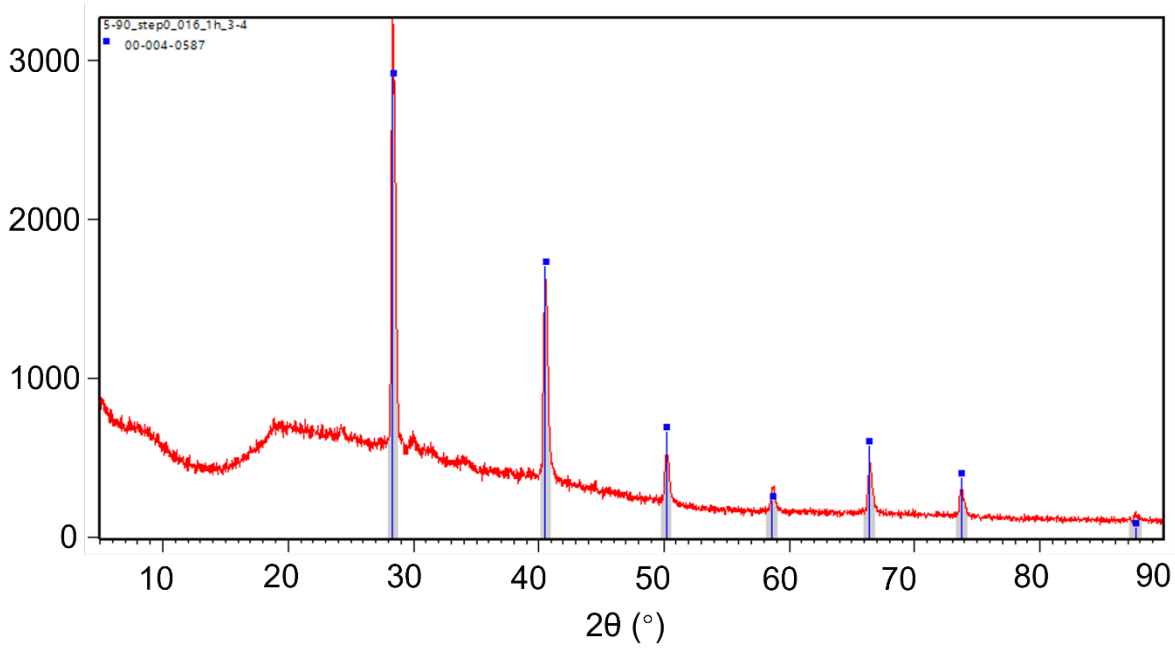

Visible	Ref. Code	Score	Compound Name	Displ.(°2θ)	Scale Fac.	Chem. Formula
1	00-004-0587	81	Potassium Chloride	0.000	0.882	KCl

Supplementary Fig. 40 and Supplementary Table 21 | PXRD pattern analysis of the KOH-WPI AF microbeads after desorption (15th) according to the ICSD database.

Section 20. Molecular Dynamics (MD) Calculations

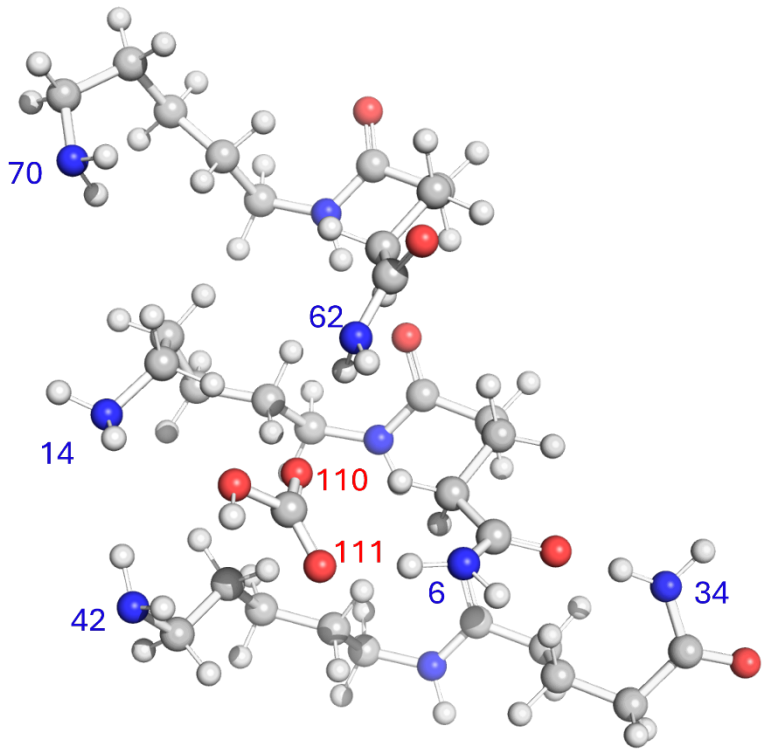

Supplementary Fig. 41 | Selected three-layer molecular model containing adjacent Lys and Gln residues in each layer for MD simulation. The oxygen of the carbonyl group is marked 110; the oxygen of the hydroxyl group is marked 111; the hydrogen of the amide group in Gln is marked 6. The red sphere is a carbon atom, the blue sphere is a nitrogen atom, the gray sphere is an oxygen atom, and the white sphere is a hydrogen atom.

578 **Supplementary Table 22 | Hydrogen bond information between the carbonyl oxygen ($O_{110\text{-carbonyl}}$)**
579 **and hydrogen of amine and amide groups of Lys and Gln, within 1 ns simulation**
580 **time at 298 K.**

H Donor	H Acceptor	Frequency	Avg. Distance (Å)	Avg. Angle (°)
3	110	0.001	3.28	154.08
40	110	0.027	3.263	159.93
4	110	0.089	3.25	160.188
42	110	0.026	3.14	160.163
59	110	0.002	3.254	160.87
6	110	0.413	2.79	164.285
62	110	0.06	2.848	160.792
10	110	0.092	3.256	158.641
11	110	0.001	3.33	156.923
64	110	0	3.151	156.702
12	110	0.11	3.275	161.437
13	110	0.005	3.273	161.812
66	110	0.001	3.326	162.38
67	110	0.001	3.262	161.622
14	110	0.029	3.108	161.317
68	110	0	3.396	150.695
70	110	0.002	3.099	159.672
69	110	0	3.449	152.356

581

582

583 **Supplementary Table 23 | Hydrogen bond information between the hydroxyl oxygen ($O_{111\text{-}hydroxyl}$)**
584 **and hydrogen of amine and amide groups of Lys and Gln within 1 ns simulation**
585 **time at 298 K.**

H Donor	H Acceptor	Frequency	Avg. Distance (Å)	Avg. Angle (°)
40	111	0.018	3.269	158.403
4	111	0.016	3.272	161.174
41	111	0	3.264	171.551
42	111	0.131	3.073	162.321
59	111	0.001	3.264	158.937
60	111	0.001	3.32	162.619
6	111	0.074	2.8	162.588
62	111	0.05	2.808	163.118
10	111	0.014	3.223	158.105
11	111	0.002	3.289	159.083
12	111	0.083	3.248	160.401
13	111	0	3.208	160.825
66	111	0.027	3.288	161.956
14	111	0.116	3.084	160.5
67	111	0.004	3.277	160.221
68	111	0.012	3.287	160.306
69	111	0.006	3.288	162.567
70	111	0.023	3.072	161.638

586

587

588 **Supplementary Table 24 | Hydrogen bond information between the carbonyl oxygen ($O_{110\text{-carbonyl}}$)**
589 **and hydrogen of amine and amide groups of Lys and Gln, within 1 ns simulation**
590 **time at 333 K.**

H Donor	H Acceptor	Frequency	Avg. Distance (Å)	Avg. Angle (°)
36	110	0.004	2.943	158.188
38	110	0.034	3.263	161.035
3	110	0.006	3.267	158.317
39	110	0.013	3.266	160.988
40	110	0.028	3.276	160.119
4	110	0.005	3.27	158.609
41	110	0.005	3.327	160.553
42	110	0.019	3.168	160.995
59	110	0	3.352	156.558
6	110	0.237	2.778	164.046
62	110	0.01	2.822	161.659
10	110	0.005	3.247	158.431
11	110	0.001	3.213	161.414
64	110	0	3.231	160.279
12	110	0.039	3.309	161.619
31	110	0.138	3.237	159.144
13	110	0	3.458	155.306
32	110	0.001	3.232	157.978
14	110	0.024	3.09	160.988
67	110	0.002	3.366	157.737
68	110	0	3.247	171.715
34	110	0.223	2.788	163.463
70	110	0.001	3.228	159.621
69	110	0.001	3.35	161.769

591

592

Supplementary Table 25 | Hydrogen bond information between the hydroxyl oxygen ($O_{111\text{-}hydroxyl}$) and hydrogen of amine and amide groups of Lys and Gln within 1 ns simulation time at 333 K.

H Donor	H Acceptor	Frequency	Avg. Distance (Å)	Avg. Angle (°)
36	111	0.001	3.036	157.682
38	111	0.014	3.257	158.809
3	111	0.001	3.244	158.68
39	111	0.007	3.285	160.927
40	111	0.022	3.254	160.523
4	111	0	3.242	160.175
41	111	0.006	3.304	161.077
42	111	0.044	3.154	161.011
60	111	0	3.341	159.522
6	111	0.03	2.778	162.263
8	111	0	3.288	159.913
62	111	0.004	2.817	161.887
10	111	0	3.289	153.744
11	111	0.008	3.276	162.02
64	111	0	3.172	158.9
12	111	0.023	3.228	158.781
31	111	0.008	3.272	159.092
66	111	0	3.344	160.442
13	111	0.001	3.291	160.501
32	111	0.005	3.236	157.484
14	111	0.128	3.061	161.252
67	111	0.002	3.27	160.074
68	111	0.002	3.241	157.838
34	111	0.235	2.777	165.018
70	111	0.009	3.03	162.424
69	111	0.002	3.246	160.407

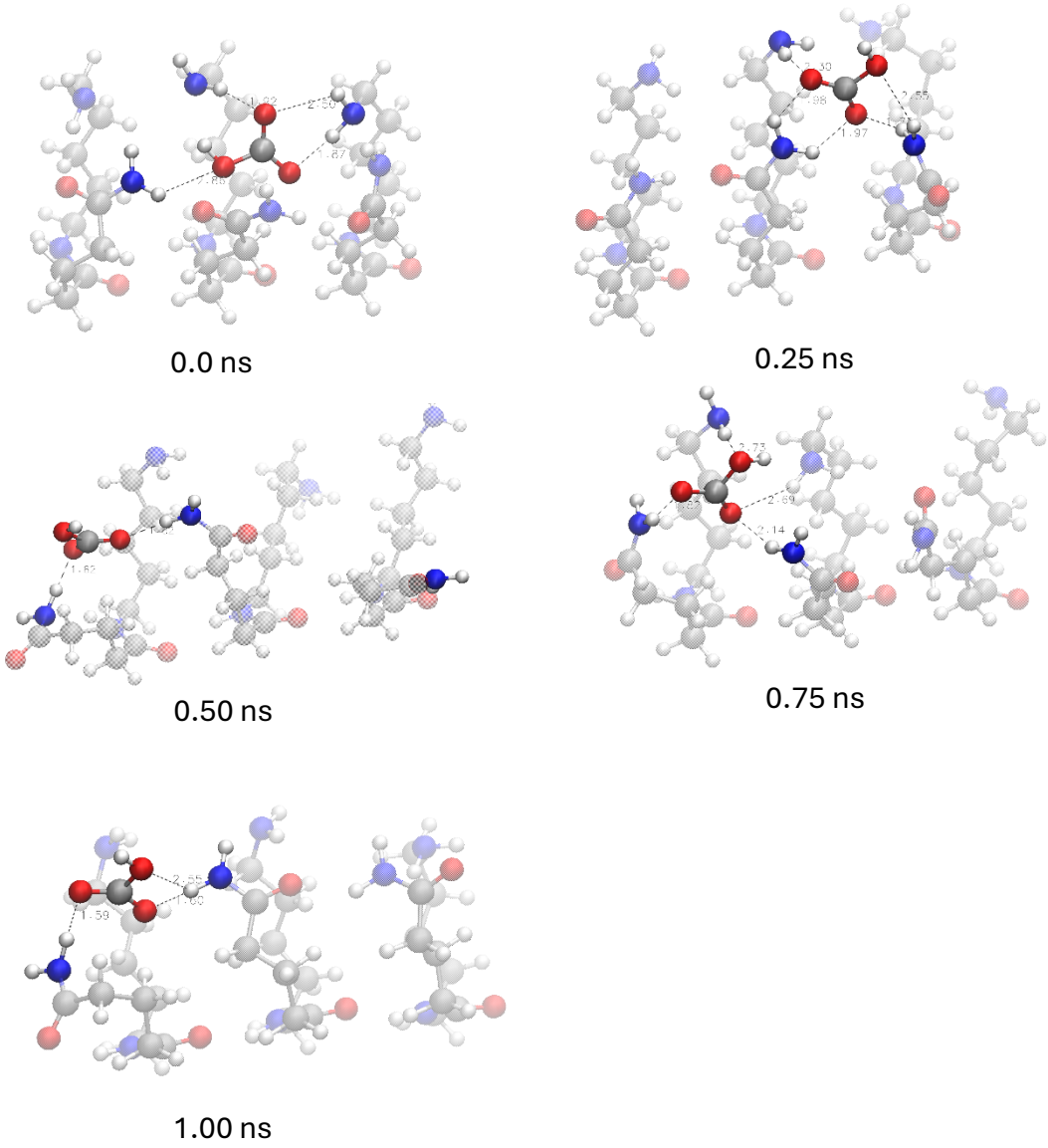

Supplementary Fig. 42 | Snapshots from MD simulation of stabilization process between bicarbonate and the selected AF cluster within 1 ns at 333 K. The VMD snapshot was taken at 0 ns, 0.25 ns, 0.5 ns, 0.75 ns, and 1 ns.

Section 21. Reduced Density Gradient (RDG) Measurement

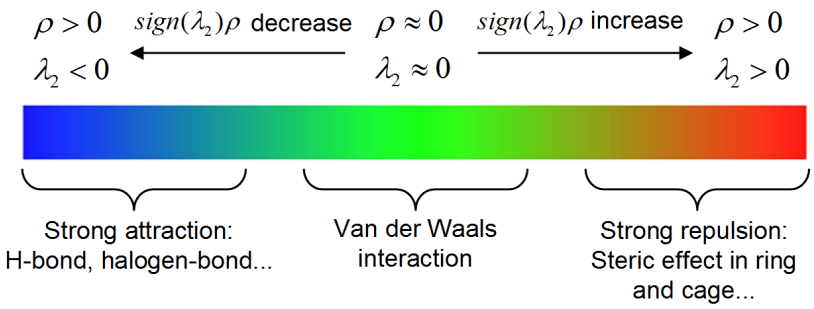

Supplementary Fig. 43 | Representative example of RDG color mapping. The blue, green, and red represent hydrogen bonding, van der Waals forces, and electrostatic interactions.

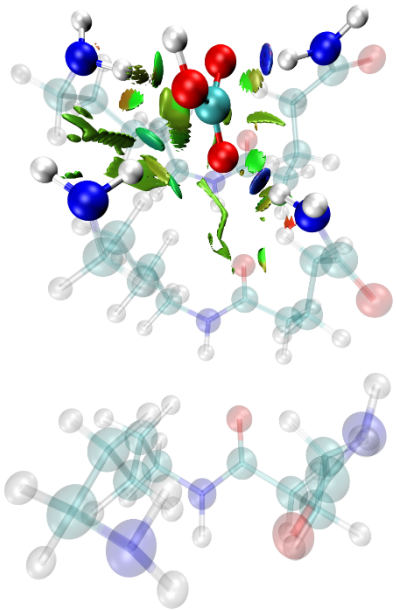

0 ns

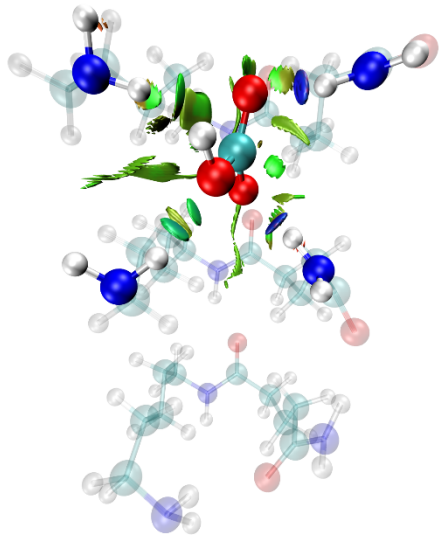

1 ns

Supplementary Fig. 44 | Two selected snapshots of RDG analysis at 298 K over 1 ns.

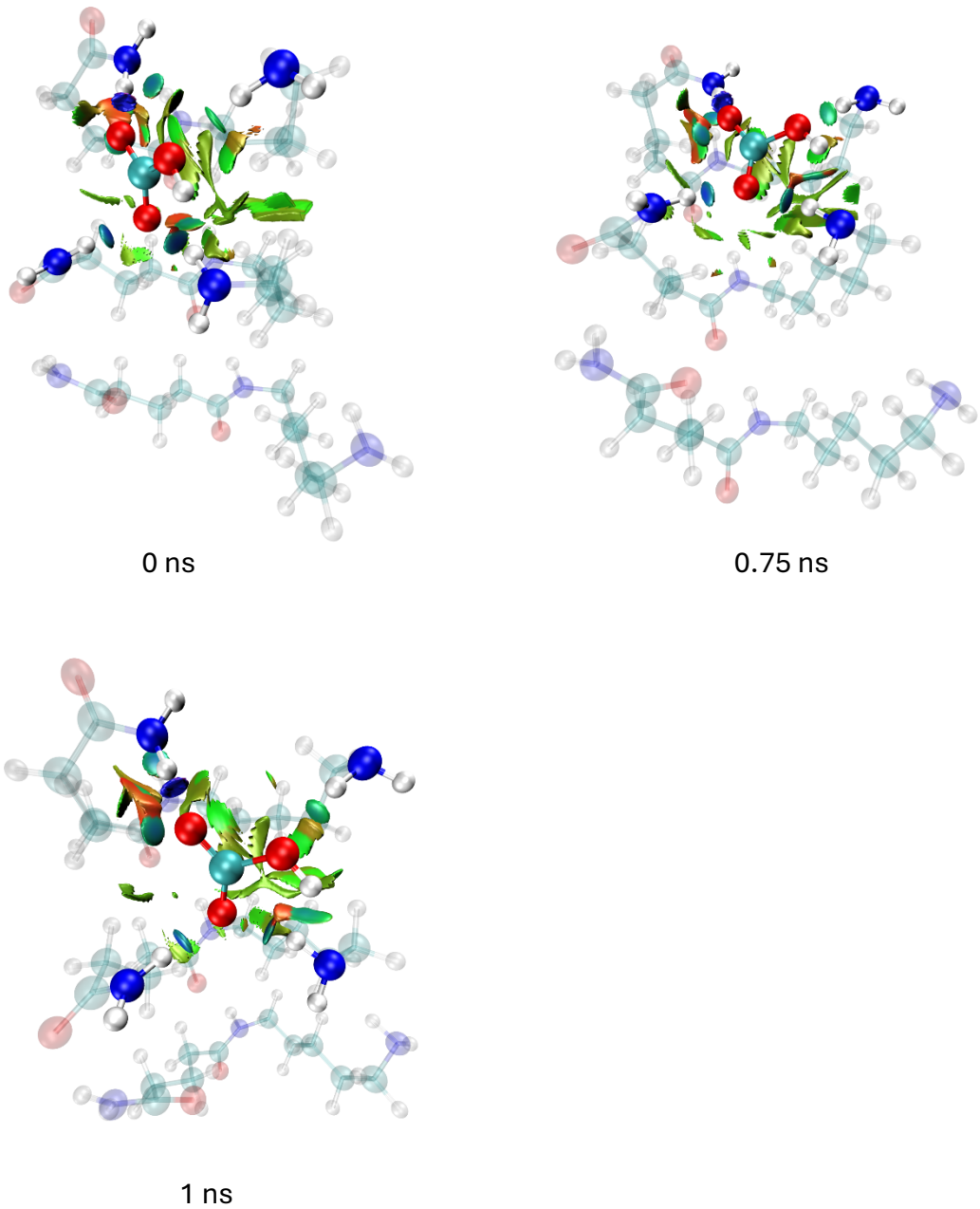

Supplementary Fig. 45 | Three selected snapshots of RDG analysis at 333 K over 1 ns.

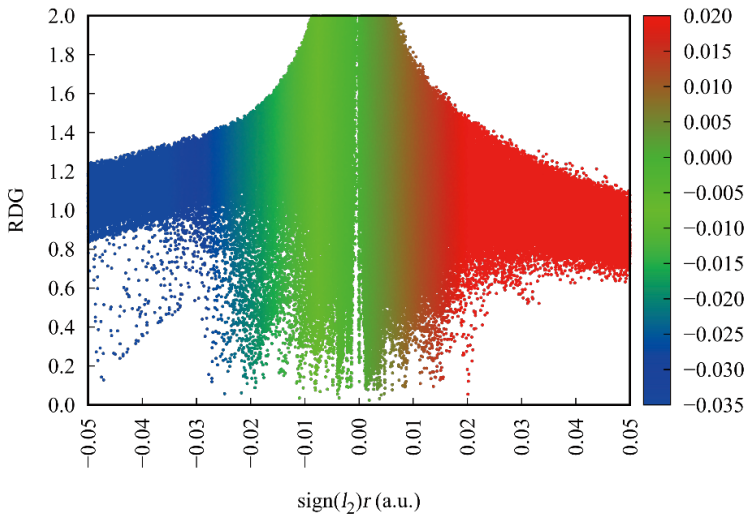

Supplementary Fig. 46 | RDG analysis of the molecular interaction at 333 K at 0.75 ns.

Section 22. Life Cycle Assessment (LCA)

22.1 Target and scope definition

(1) Target

This study applies the Life Cycle Assessment (LCA) method based on the ISO 14040/14044 standards, with DAC as the application scenario. It compares the environmental impacts of different amine-modified sorbents, including AEAPDMS-NFC, PEI/TEPA-SBA-15, and COF under the same functional unit, providing a basis for the development of eco-friendly DAC sorbents.

(2) Functional unit

The selection of a functional unit for DAC should account for material durability and energy efficiency under realistic operating conditions. Here, we define the functional unit as "the sorbent required to capture 1 kg CO_2 from air across 20 operating cycles. This definition enables reasonable comparison between sorbent materials by evaluating long-term performance rather than single-cycle capacity, which is critical for assessing environmental and economic feasibility. The 20-cycle timeframe also captures potential degradation and stability effects that may not emerge in shorter tests, providing a more comprehensive basis for life cycle assessment and technology evaluation. The cyclic performance across 20 cycles of each selected sorbent is obtained from the publications (**Supplementary Tables 3−6**).

To meet the defined functional unit, 0.53 kg of AF microbeads is required, based on an average CO_2 uptake of 2.0 mmol g^{-1} across 20 cycles. By contrast, aminosilane-modified NFC requires 32.71 kg due to the intensive chemical pretreatment for cellulose recovery and amine modification, coupled with its lower average uptake (0.70 mmol g^{-1}), reflecting a 50% capacity loss over 20 cycles. For comparison, 50% PEI/SBA-15, 50% TEPA/SBA-15, and COF require 0.85, 0.50, and 0.55 kg, respectively, reflecting uptake capacities of 1.34, 2.30, and 2.05 mmol g^{-1} across 20 cycles. To standardize energy accounting, the reported synthesis processes, including drying and calcination, were assumed to be conducted using the same laboratory equipment (hot plate, oven, refrigerator, freeze dryer, and rotary evaporator).

(3) System boundary

The system boundary for the LCA of DAC sorbents is defined as sorbent production from raw materials followed by DAC operation across 20 cycles. For AF-based sorbents, this includes AF assembly from whey and alkali functionalization. For NFC-, silica-, and COF-supported sorbents, the synthesis of precursors together with subsequent amine modification is considered.

In all cases, electricity inputs for the above processes, as well as for thermal and acid-hydroxide mist regeneration, are included within the boundary.

(4) Cut-off criteria

Based on the defined system boundary, data collection in this study follows four criteria:

(A) Foreground data should include all primary material and energy inputs for each unit process.

(B) Auxiliary materials (e.g., wastewater treatment reagents or trace additives) accounting for <1% of total material consumption may be excluded, provided their cumulative share does not exceed 5%.

(C) General solid waste representing <1% of total emissions may be excluded.

(D) Infrastructure (roads, buildings), process equipment, and consumption or emissions associated with personnel and living facilities are excluded.

22.2 Process data collection

Supplementary Table 26 | Consumption of material and energy of KOH-AF microbead production and regeneration for capturing 1 kg CO_2 from ambient air with 20 cycles.

	Items	Quantities	Unit
Material consumption	Whey protein isolate	0.51	kg
	Hydrochloric acid	0.11	kg
	Potassium hydroxide	0.11	kg
	Water	433.05	L
Energy consumption	Fibrilization	1.20	kWh
	Bead synthesis	38.74	kWh
	20-cycle operation	0.15	kWh
Product outputs	Fibril microbead	0.53	kg

748 **Supplementary Table 27 | Consumption of material and energy of AEAPDMS-NFC[17,24]**
749 **production and regeneration for capturing 1 kg CO_2 from ambient air with 20 cycles.**

	Items	Quantities	Unit
Material consumption	For AEAPDMS (3-aminopropylmethyldiethoxysilane) synthesis		
	γ-chloropropyl-methyldichlorosilane	0.072	kg
	γ-chloropropyl-methyldiethoxysilane	1.89	kg
	Potassium iodide	0.0090	kg
	Dry ammonia	3.84	kg
	Sodium methylate	0.15	kg
	Ethanol	4.43	kg
	For NFC (Nanofibrillated Cellulose) synthesis		
	Bleached kraft pulp	40.82	kg
	Deionized water	3586	L
	Sodium hydroxide	34.23	kg
	Carboxymethylcellulose	4.40	kg
Energy consumption	NFC production	840	kWh
	Freeze-drying	80	kWh
	Thermal treatment	50	kWh
	20-cycle operation	100.0	kWh
Product outputs	AEAPDMS-NFC-FD cryogel	32.71	kg

750

751

752 **Supplementary Table 28 | Consumption of material and energy of 50% TEPA/SBA-15**[20]
753 **production and regeneration for capturing 1 kg CO_2 from ambient air with 20 cycles.**

	Items	Quantities	Unit
Material consumption	For SBA-15 synthesis		
	Pluronic P123	0.32	kg
	TEOS	0.62	kg
	HCl (36%)	1.89	kg
	Deionized water	8.5	kg
	For amine loading		
	TEPA	0.25	kg
	Methanol	9.81	kg
Energy consumption	SBA-15 Synthesis	467.3	kWh
	TEPA Impregnation	3.28	kWh
	20-cycle operation	99.0	kWh
Product outputs	50% TEPA/SBA-15	0.85	kg

754

755

Supplementary Table 29 | Consumption of material and energy of 50% PEI/SBA-15[20] production and regeneration for capturing 1 kg CO_2 from ambient air with 20 cycles.

	Items	Quantities	Unit
Material consumption	For SBA-15 synthesis		
	Pluronic P123	0.55	kg
	TEOS	0.11	kg
	HCl (36%)	3.24	kg
	Deionized water	14.5	kg
	For amine loading		
	PEI	0.43	kg
	Methanol	16.80	kg
Energy consumption	SBA-15 Synthesis	799.80	kWh
	PEI Impregnation	4.71	kWh
	20-cycle operation	100.60	kWh
Product outputs	50% TEPA/SBA-15	0.50	kg

Supplementary Table 30 | Consumption of material and energy of COF[23] production and regeneration for capturing 1 kg CO_2 from ambient air with 20 cycles.

	Items	Quantities	Unit
Material consumption	**COF-999-N_3 Synthesis:**		
	TCPB((1,3,5-tris(4-cyanomethylphenyl)benzene))	0.26	kg
	BPDA-N_3 (3,3′-bis[(6-azidohexyl)oxy]-4,4′-biphenyldicarbaldehyde)	0.46	kg
	Cs_2CO_3 (cesium carbonate)	0.60	kg
	1,2-dichlorobenzene	10.041	kg
	1-butanol	6.24	kg
	Methanol	365.67	kg
	COF-999-NH_2 Synthesis:		
	PPh_3 (triphenylphosphine)	1.11	kg
	Methanol	210.83	kg
	Water	33.20	kg
	Methanol	16.80	kg
	COF-999 Functionalization:		
	Toluene	26.70	kg
	Acetic acid	0.081	kg
	Aziridine	1.28	kg
	1 M NaOH in methanol	609.37	kg
	Methanol	79.20	kg
Energy consumption	COF-999-N_3 Synthesis	907.40	kWh
	COF-999-NH_2 Synthesis	367.40	kWh
	COF-999 Functionalization	1,338.90	kWh
	20-cycle operation	40.0	kWh
Product outputs	COF-999	0.55	kg

22.3 Life cycle impact assessment (LCIA)

(1) Impact assessment method

The LCIA is conducted using the ReCiPe 2016 V1.10 midpoint (H) impact assessment method, which includes 18 environmental impact indicators.

Supplementary Table 31 | Environmental impact indicators categories for LCA.

Impact category	Unit
Global warming	kg CO_2 eq
Stratospheric ozone depletion	kg CFC11 eq
Ionizing radiation	kBq Co-60 eq
Ozone formation, Human health	kg NO_x eq
Fine particulate matter formation	kg PM2.5 eq
Ozone formation, Terrestrial ecosystems	kg NO_x eq
Terrestrial acidification	kg SO_2 eq
Freshwater eutrophication	kg P eq
Marine eutrophication	kg N eq
Terrestrial ecotoxicity	kg 1,4-DCB
Freshwater ecotoxicity	kg 1,4-DCB
Marine ecotoxicity	kg 1,4-DCB
Human carcinogenic toxicity	kg 1,4-DCB
Human non-carcinogenic toxicity	kg 1,4-DCB
Land use	m^2a crop eq
Mineral resource scarcity	kg Cu eq
Fossil resource scarcity	kg oil eq
Water consumption	m^3

(2) Impact assessment results

Supplementary Table 32 | Comparison of LCIA results between AF microbead and selected four sorbents for capturing 1 kg CO_2 from ambient air with 20 cycles.

Impact category	Unit	This work	AEAPDMS-NFC	PEI/SBA-15	TEPA/SBA-15	COF
Global warming	kg CO_2 eq	22.82354483	1098.3367	709.22089	447.94778	3421.81974
Stratospheric ozone depletion	kg CFC11 eq	3.42203E-05	0.000362491	0.0002326	0.000147643	0.00089398
Ionizing radiation	kBq Co-60 eq	1.693063999	66.56292	78.952494	49.748102	249.757763
Ozone formation, Human health	kg NO_x eq	0.052622417	2.4043065	1.6142727	1.0193991	7.17086086
Fine particulate matter formation	kg PM2.5 eq	0.042934053	1.7002477	1.4210086	0.8968314	5.18212854
Ozone formation, Terrestrial ecosystems	kg NO_x eq	0.054070925	2.525533	1.6534097	1.0437564	7.71951491
Terrestrial acidification	kg SO_2 eq	0.097870259	3.3150415	2.3713933	1.4978141	9.12443574
Freshwater eutrophication	kg P eq	0.010534155	0.54518094	0.4095353	0.25831168	1.47614375
Marine eutrophication	kg N eq	0.005366405	0.03882813	0.0244159	0.015362818	0.10771758
Terrestrial ecotoxicity	kg 1,4-DCB	118.3167207	8956.3156	2573.6473	1700.0016	19647.4165
Freshwater ecotoxicity	kg 1,4-DCB	1.324511615	50.887576	43.233012	27.273641	149.714212
Marine ecotoxicity	kg 1,4-DCB	1.776645567	74.14742	56.738599	35.880911	208.279418
Human carcinogenic toxicity	kg 1,4-DCB	3.389784056	147.71579	81.425163	51.417715	402.740701
Human non-carcinogenic toxicity	kg 1,4-DCB	27.25549646	1119.9162	834.59406	526.80007	2958.50153
Land use	m^2a crop eq	23.04132398	56.562695	14.913096	9.4051898	57.935383
Mineral resource scarcity	kg Cu eq	0.06953164	2.6167137	1.2557484	0.79497536	6.22842128
Fossil resource scarcity	kg oil eq	5.1748631	340.28618	187.52261	118.24692	1706.4028
Water consumption	m^3	0.68296118	39.18485	4.5131879	2.9011939	18.3424054

(3) Interpretation of LCIA results

The LCIA results show that, under the same functional unit (capturing 1 kg CO_2 under 20 cycles) and comparable system boundary conditions, the AF microbead exhibits a significantly lower environmental impact than the amine-based sorbents. Among the 18 selected environmental impact indicators, AF microbead demonstrates unparalleled environmental performance, with impacts reduced by more than 95–99% across nearly all categories when benchmarked against NFC (set to 100%). Even when compared with established amine–silica sorbents, this work consistently delivers an order of magnitude lower burdens, underscoring its potential as a truly sustainable DAC material[25].

For eutrophication, this work records only 0.71% of NFC in freshwater and 4.99% in marine systems, representing reductions of more than 99% relative to NFC and at least 4–7 times lower impacts than PEI-silica (22–36%) and TEPA-silica (18–28%). Resource consumption is also minimized: water use accounts for 1.74% of NFC, compared with 7–12% for amine-silica. Mineral resource scarcity is only 1.12%, nearly 20–40 × lower than PEI-silica (42.0%) and TEPA-silica (20.2%). Fossil resource use falls to 0.30%, confirming a 97–99% advantage.

Similar margins reduce human health impacts. Carcinogenic toxicity is 0.84% of NFC, versus 20–37% for amine–silica. Non-carcinogenic toxicity remains at 0.92%, compared with 28–38% for silica-based sorbents. Freshwater and marine ecotoxicity are reduced to ~0.85–0.88%, at least 30 × lower than TEPA-silica and PEI-silica.

Air-quality indicators show the same pattern. Fine particulate matter formation is 0.83%, while ozone formation (human health) is 0.73%, both far below TEPA-silica (22–27%) and PEI–silica (33%).

Climate-related burdens further highlight the advantage. The global warming impact is only 0.67% of NFC, more than 30 times lower than amine–silica. Stratospheric ozone depletion is 3.83%, still an order of magnitude below silica benchmarks.

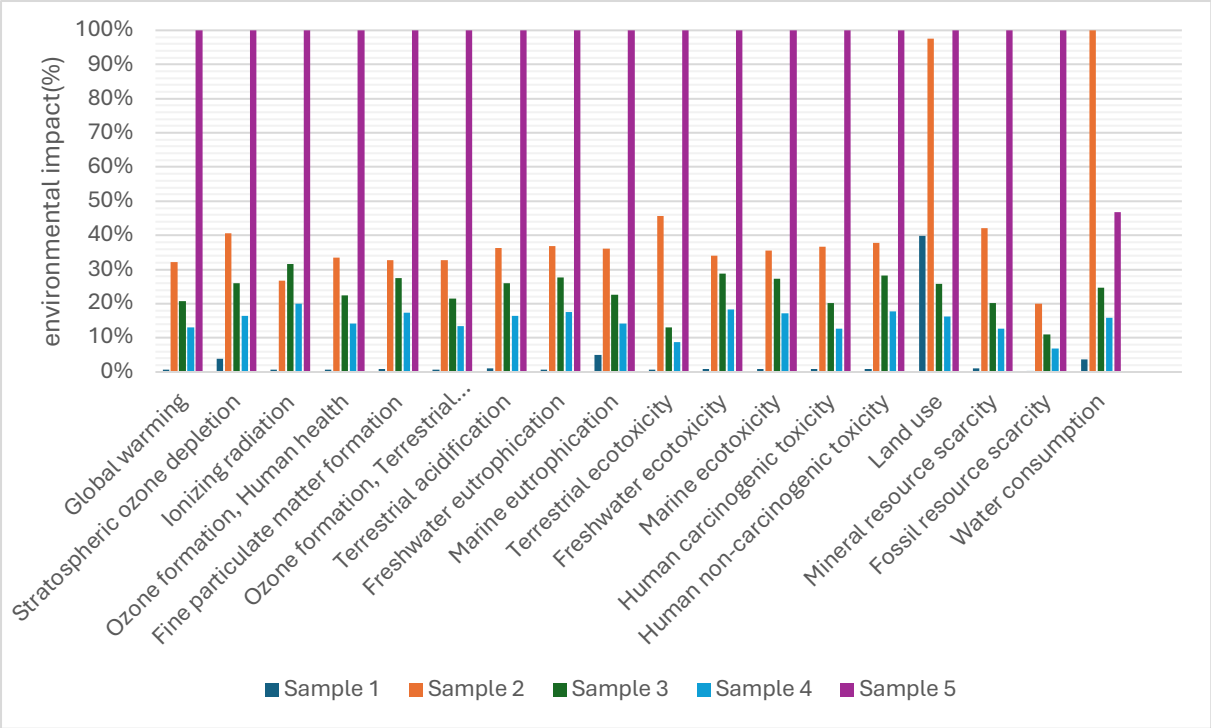

Supplementary Fig. 47 | Bar diagram of the LCA results. Samples 1, 2, 3, 4, and 5 represent this work, AEAPDMS-NFC, TEPA/SBA-15, PEI/SBA-15, and COF, respectively.

Section 23. Biodegradability Test

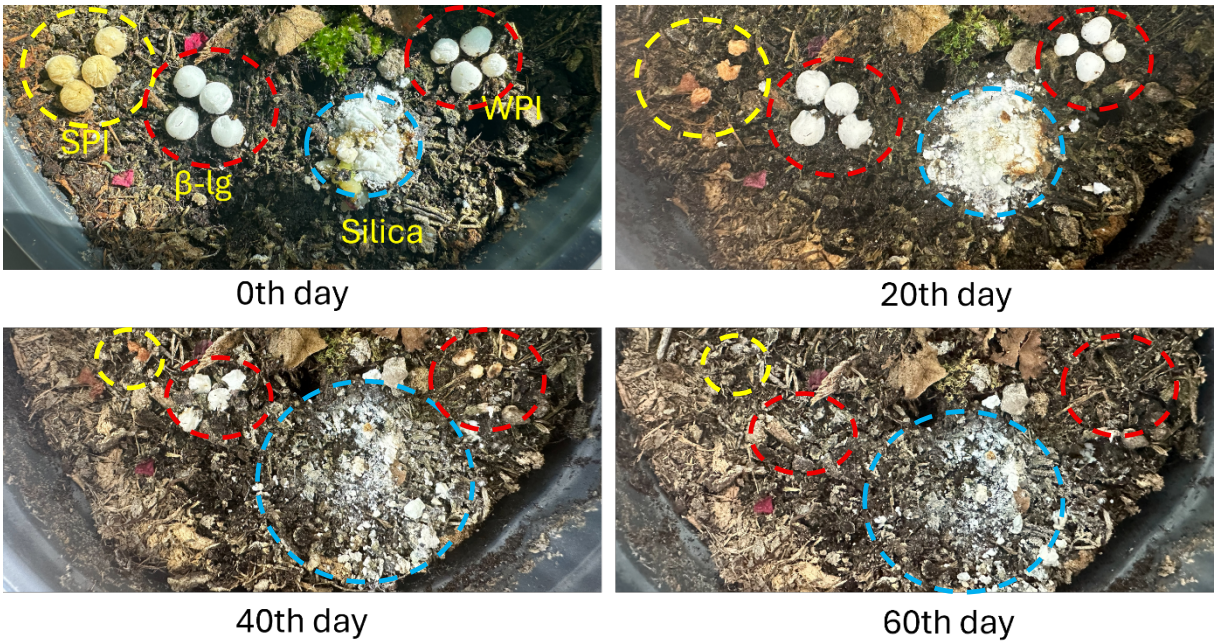

Supplementary Fig. 48 | Biodegradability of KOH-modified SPI, *β*-lg, WPI AF microbeads, and PEI-grafted mesoporous silica. The tested material was placed on the soil surface in an indoor flower pot for full exposure to ambient air (~420 ppm CO_2, 28–30 °C, 30–40% RH) during June–August 2025. To minimize the influence of water on degradation, watering was limited to once every two to three weeks. Note that the drying of the soil was caused by high temperature and water insufficiency.

Section 24. The Ranking Efficiency Product (REP)

24.1 Definition and calculation

To enable a more systematic and comparable assessment of CO_2 capture, we rely on the compact index provided by the ranking efficiency product (REP)[26], which integrates normalized scores of the six main assessement key criteria, such as: i) adsorption capacity, ii) regeneration temperature, iii) regeneration time, iv) cycling stability, v) production cost, vi) sustainability (glo from the LCA analysis). This composite metric provides a quantitative basis for benchmarking different CO_2 capture technologies, facilitating the evaluation of trade-offs between their respective advantages and limitations.

To calculate the REP value for any (j) of the CO_2 capture technologies considered, we use the following equation[26].

$$REP_j = \left[\prod_i^n \left({}^{r_i}/_{r_{i-MAX}}\right)_j\right]^{1/n}$$

Where r_i is the individual ranking score for the characteristic i of the CO_2 capture technology j under scrutiny. According to this simple approach, a technology j can be evaluated by ranking each i of the n independent characteristics (6 in the present case) between a minimum r_{i-MIN} and a maximum rank, r_{i-MAX} . REP as defined above varies between (r_{i-MIN}/r_{i-MAX}) and 1, for the worst and best performing technologies, respectively. The individual values from which r_i are calculated are given in Supplementary Fig. 49. Individual literature values are ranked on linear scales and normalized, to vary between 1 (minimum score) and 5 (maximum score).

24.2 Calculation boundaries

Following the sustainability framework of our previous work[26], technological sustainability should be assessed not solely by CO_2 capture capacity but through a comprehensive analysis of environmental, energetic, and economic factors[27]. To ensure a unified and quantitative comparison across sorbents with differing physicochemical and operational characteristics, each parameter was linearly normalized to a five-point scale (1−5), where 5 represents the best achievable performance and 1 the least favorable. The scaling references were fixed according to experimentally or literature-validated benchmarks. The CO_2 uptake capacity was linearly scaled between 1.34 mmol g^{-1} (1 point) and 2.30 mmol g^{-1} (5 points)[28]. The desorption temperature was inversely rated from 25 °C (5 points) to 120 °C (1 point), and the desorption time from 11 min (5 points) to 60 min (1 point). The cycling stability was proportionally scaled up to 100 cycles (5 points). The capture cost was inversely scaled using the experimentally derived cost to capture 1 kg CO_2 over 20 cycles (**Section 22.2**), with 3.04−8.64 € kg^{-1} CO_2 (8.64 € for 5 points) for the KOH-AF microbeads and proportionally lower scores up to 1119.78 € kg^{-1} CO_2 (1 point) for the most energy-intensive COF system. Finally, the life-cycle CO_2 emission (kg CO_2 eq per kg CO_2 captured) was inversely scaled between 22.8 (5 points) and 3421.82 (1 point). The overall sustainability index ($REP_{(1-5)}$) was then calculated as the geometric mean of the six normalized scores, integrating environmental, energetic, and economic contributions into a single dimensionless indicator.

Using this multi-criteria REP analysis, the KOH–AF microbeads exhibited the highest overall sustainability (REP ≈ 0.80) among representative thermally regenerable DAC sorbents (**Supplementary Fig. 49**). Crucially, their CO_2 uptake of 2.20 mmol g^{-1} was measured under real ambient air (~420 ppm CO_2, ~21 % O_2, 40–55% RH), whereas the comparison sorbents, such as AEAPDMS-NFC and PEI/TEPA-silica, were tested in O_2-free simulated air, conditions that overestimate amine performance by suppressing oxidative degradation. Even under these more demanding, realistic conditions, the AF microbeads achieved thermal-free regeneration (25 °C, ~11 min), outperforming heat-driven COF and amine–silica systems (60–120 °C). Their high REP arises from the synergy of low-temperature, rapid regeneration, minimal life-cycle CO_2 emissions (22.8 kg CO_2-eq kg^{-1} CO_2), and low capture cost (8.64 € kg^{-1} CO_2 over 20 cycles). In contrast, COF-999 and AEAPDMS–NFC display much higher embodied emissions (≈ 1100−3400 kg CO_2-eq kg^{-1} CO_2) and costs (≈ 280−1120 € kg^{-1} CO_2), yielding markedly lower REP values (0.45−0.52). Analogous to adsorption technologies in sustainable water purification, these results highlight that waste-protein-derived amyloid-fibril sorbents, built

from circular, biodegradable feedstocks, can rival, and, when evaluated under realistic ambient-air conditions, surpass synthetic frameworks in overall sustainability, situating them within the most sustainable quadrant of the DAC landscape.

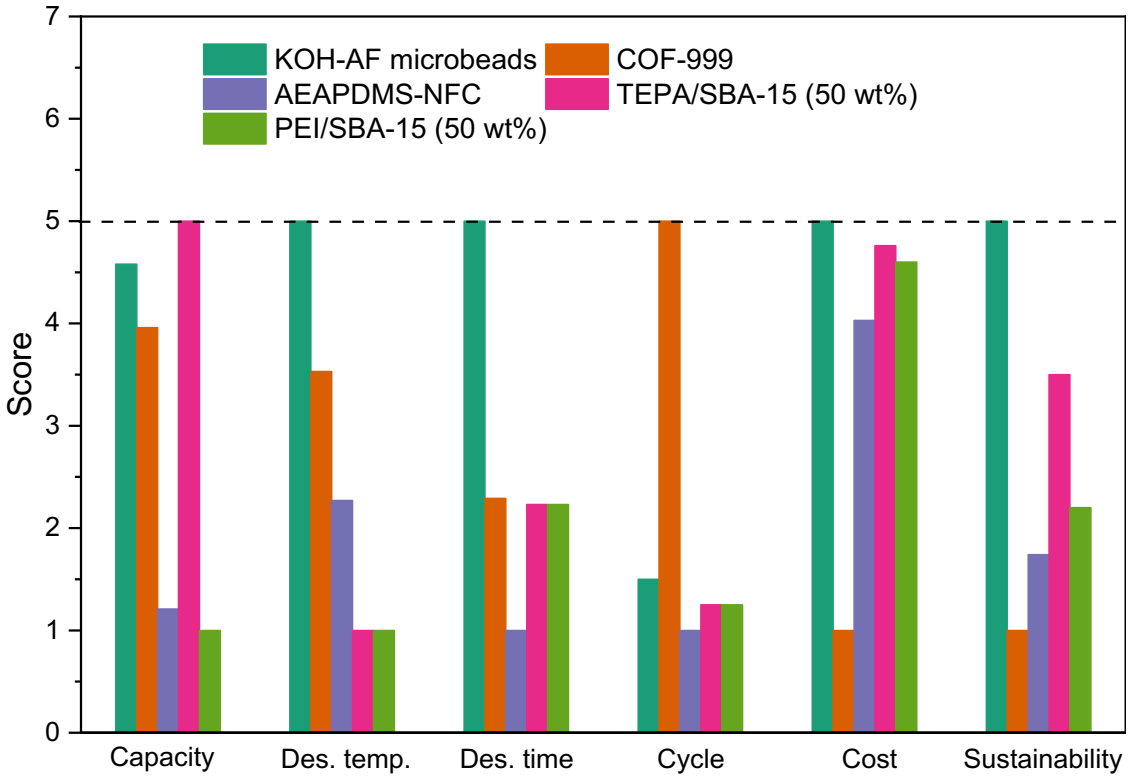

Supplementary Fig. 49 | A comparison of the technological edges of KOH-WPI AF microbeads with sorbents described in the LCA section according to the rank product statistics. 1 and 5 correspond to the worst and best performance, respectively.

Section 25. Techno-Economic Assessment (TEA)

Supplementary Table 33 | Cost analysis for KOH-WPI AF microbeads for capturing 1 kg and 1 ton CO_2 from air.

	Price	Unit	input	unit
Whey protein	0.80–1.40	EUR/kg	3.80[b]	kg
HCl	0.4233	EUR/kg	0.11	kg
NaOH	0.382	EUR/kg	0.11	kg
Water	8.08E-05	EUR/kg	433.05	kg
Electricity	0.1070	EUR/kWh	12.45	kWh
Total cost	3.04	EUR	1	kg CO_2
	3.58[c]	USD		
	342[d]	EUR	1	ton CO_2
	372	USD		

a, lower-end animal feed grade whey powder.

b, The raw whey powder required to obtain 0.506 g WPI isolate.

c, The value in EUR was converted to US$2022 terms using annual exchange rates from the International Monetary Fund (IMF)[27]

d, Adsorbent consumption is assumed to be 3.80 kg under 3000 cycles, 3.6 kWh per cycle, and CO_2 uptake is assumed to be 2.0 mmol g^{-1}.

Section 26. Roasted Coffee Bean Degassing

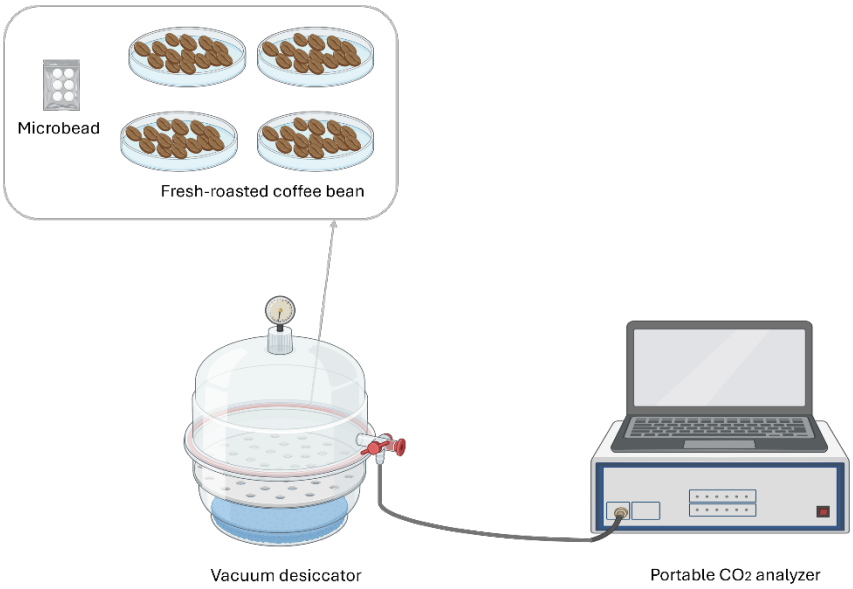

Supplementary Fig. 50 | Schematic diagram of CO_2 removal experiments using KOH-AF WPI microbeads for freshly roasted coffee beans. Freshly roasted coffee beans were purchased from a local coffee shop. The coffee beans without any treatment served as the blank.

Supplementary Fig. 51 | Comparison of in-pack gas volume during coffee bean storage. Each bag contained 50 g of freshly roasted coffee beans. Commercial coffee packaging typically employs a one-way degassing valve to vent CO_2 while restricting O_2 ingress. To isolate the effects of gas capture, the freshly roasted beans were sealed without prior degassing or N_2 purging. In this valveless configuration, a commercial oxygen adsorbent was included to minimize the influence of residual O_2 on pouch swelling, for example, from lipid oxidation. **a**, Without any sorbent, the bag exhibited pronounced swelling, primarily due to CO_2 evolution and residual O_2. **b**, With only the oxygen adsorbent, swelling was reduced but remained evident because CO_2 was neither vented nor captured. **c**, When both the oxygen adsorbent and CO_2-capturing microbeads were included, the bag showed the smallest headspace volume, consistent with simultaneous O_2 removal and CO_2 sequestration by the microbeads[29].

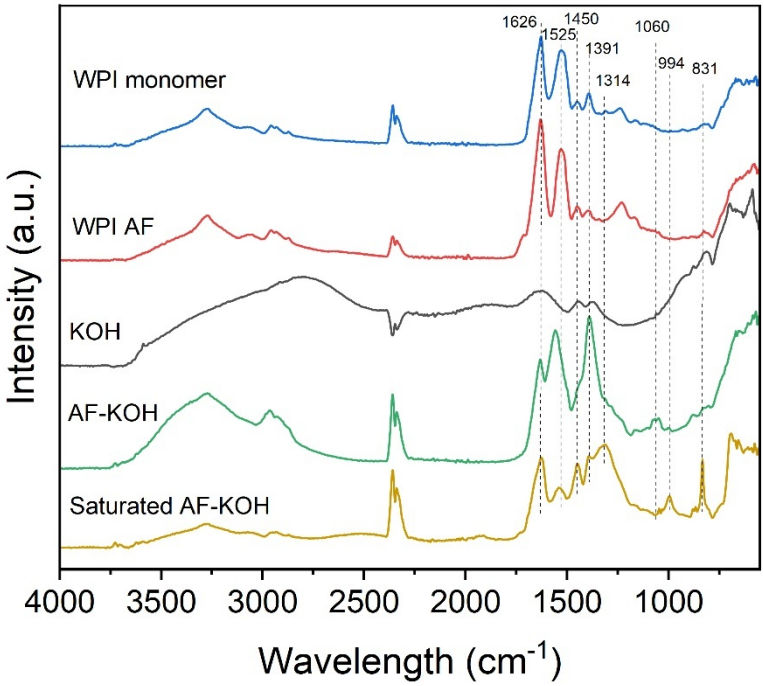

Supplementary Fig. 52 | FT-IR spectra of KOH-WPI AF microbead before and after coffee bean degassing experiment.

928 ## Section 27. In vitro Simulated Digestion

929 **Supplementary Table 34 | Free amino acid analysis of pure AF microbeads after simulated**
930 **in vitro digestion**. The values are representative of three independent replicates (n = 3).

Pure AF microbead	
Item	Amino acid content (mg g^{-1})
Asp	115.76, 112.41, 116.81
Thr	43.84, 46.00, 44.7
Ser	41.87, 39.67, 43.42
Glu	192.75, 176.56, 192.91
Pro	52.73, 53.31, 54.61
Gly	34.65, 36.39, 35.82
Ala	40.26, 38.79, 41.09
Cys	20.49, 20.64, 20.76
Val	33.15, 31.81, 32.96
Met	12.06, 10.85, 11.88
Ile	27.43, 28.6, 27.28
Leu	75.49, 71.14, 76.65
Tyr	19.30, 17.54, 19.35
Phe	25.12, 23.69, 25.16
Lys	63.86, 60.52, 67.05
His	15.45, 16.28, 15.90
Arg	17.25, 17.47, 16.59

931

932

933 **Supplementary Table 35 | Free amino acid analysis of spent KOH-WPI AF microbeads**
934 **from in-pack experiment after simulated in vitro digestion.** The values are representative of
935 three independent replicates (n = 3).

CO_2-saturated AF microbeads	
Item	Amino acid content (mg g^{-1})
Asp	99.02, 91.52, 108.49
Thr	38.66, 38.29, 39.18
Ser	41.15, 44.58, 39.86
Glu	156.69, 169.92, 146.79
Pro	62.44, 63.92, 62.25
Gly	42.09, 42.2, 43.46
Ala	35.44, 36.95, 35.84
Cys	15.69, 15.42, 16.44
Val	27.92, 28.88, 27.41
Met	9.45, 8.92, 9.96
Ile	27.11, 27.06, 27.2
Leu	61.73, 60.55, 62.71
Tyr	17.69, 16.94, 18.16
Phe	22.85, 23.17, 22.48
Lys	44.63, 43.65, 44.58
His	12.95, 13.46, 11.92
Arg	15.39, 14.52, 14.14

936

937

Section 28. Potential Application in Fertilizer

Supplementary Table 36 | Estimated N: K ratio of spent KOH-WPI AF microbeads.

Quantity	Value	Formula
AF mass (g)	5.00	Baseline for 5:1 example
KOH mass (g)	1.00	From AF: KOH = 5:1
Protein N content (wt%)	16.0%	Jones factor 6.25
Nitrogen mass, N (g)	0.80	0.16 × AF mass
K mass fraction in KOH	0.697	39.10/56.11
Potassium mass, K (g)	0.697	0.697 × KOH mass
N: K by mass	1.15:1 (this work)	0.80:0.697
	0.34:1 (Potassium nitrate)	
	1.20:1 (NPK 20 20 20)	

References

1. Fakhraee, M., Planavsky, N. J. & Reinhard, C. T. Ocean alkalinity enhancement through restoration of blue carbon ecosystems. *Nat. Sustain.* **6**, 1087–1094 (2023).
2. Sabine, C. L. *et al.* The Oceanic Sink for Anthropogenic CO2. *Science* **305**, 367–371 (2004).
3. Fan, M. *et al.* Structuring ZIF-8-based hybrid material with hierarchical pores by in situ synthesis and thermal treatment for enhancement of CO2 uptake. *J. Solid State Chem.* **269**, 507–512 (2019).
4. Kumar, S., de A. e Silva, J., Wani, M. Y., Gil, J. M. & Sobral, A. J. F. N. Carbon dioxide capture and conversion by an environmentally friendly chitosan based meso-tetrakis(4-sulfonatophenyl) porphyrin. *Carbohydr. Polym.* **175**, 575–583 (2017).
5. Wang, Y., Qu, L., Ding, H., Webley, P. & Li, G. K. Distributed direct air capture of carbon dioxide by synergistic water harvesting. *Nat. Commun.* **15**, 9745 (2024).
6. Hsan, N., Dutta, P. K., Kumar, S., Bera, R. & Das, N. Chitosan grafted graphene oxide aerogel: Synthesis, characterization and carbon dioxide capture study. *Int. J. Biol. Macromol.* **125**, 300–306 (2019).
7. Li, H. *et al.* Capturing carbon dioxide from air with charged-sorbents. *Nature* **630**, 654–659 (2024).
8. Zhu, Y., Booth, A. & Hatzell, K. B. Confinement Effects on Moisture-Swing Direct Air Capture. *Environ. Sci. Technol. Lett.* **11**, 89–94 (2024).
9. Chen, O. I.-F. *et al.* Water-Enhanced Direct Air Capture of Carbon Dioxide in Metal–Organic Frameworks. *J. Am. Chem. Soc.* **146**, 2835–2844 (2024).
10. Wang, T., Lackner, K. S. & Wright, A. Moisture Swing Sorbent for Carbon Dioxide Capture from Ambient Air. *Environ. Sci. Technol.* **45**, 6670–6675 (2011).
11. McDonald, T. M. *et al.* Capture of Carbon Dioxide from Air and Flue Gas in the Alkylamine-Appended Metal–Organic Framework mmen-Mg2(dobpdc). *J. Am. Chem. Soc.* **134**, 7056–7065 (2012).
12. Bien, C. E. *et al.* Bioinspired Metal–Organic Framework for Trace CO2 Capture. *J. Am. Chem. Soc.* **140**, 12662–12666 (2018).
13. CO2 capture using whey protein isolate.
14. Li, D. *et al.* Designed amyloid fibers as materials for selective carbon dioxide capture. *Proc. Natl. Acad. Sci.* **111**, 191–196 (2014).
15. Dong, Z. *et al.* Amine-Functionalized Amyloid Aerogels for CO_2 Capture. *ChemSusChem* **16**, e202300767 (2023).
16. Peydayesh, M. *et al.* Amyloid fibril-UiO-66-NH_2 aerogels for environmental remediation. *Chem. Commun.* **58**, 5104–5107 (2022).
17. Gebald, C., Wurzbacher, J. A., Tingaut, P., Zimmermann, T. & Steinfeld, A. Amine-Based Nanofibrillated Cellulose As Adsorbent for CO_2 Capture from Air. *Environ. Sci. Technol.* **45**, 9101–9108 (2011).
18. Gebald, C., Wurzbacher, J. A., Borgschulte, A., Zimmermann, T. & Steinfeld, A. Single-Component and Binary CO_2 and H_2 O Adsorption of Amine-Functionalized Cellulose. *Environ. Sci. Technol.* **48**, 2497–2504 (2014).
19. Sehaqui, H. *et al.* Fast and Reversible Direct CO_2 Capture from Air onto All-Polymer Nanofibrillated Cellulose—Polyethylenimine Foams. *Environ. Sci. Technol.* **49**, 3167–3174 (2015).
20. Miao, Y., He, Z., Zhu, X., Izikowitz, D. & Li, J. Operating temperatures affect direct air capture of CO2 in polyamine-loaded mesoporous silica. *Chem. Eng. J.* **426**, 131875 (2021).

21. Wang, J. *et al.* Direct Capture of Low-Concentration CO2 on Mesoporous Carbon-Supported Solid Amine Adsorbents at Ambient Temperature. *Ind. Eng. Chem. Res.* **54**, 5319–5327 (2015).
22. Zhu, X. *et al.* Efficient CO2 capture from ambient air with amine-functionalized Mg–Al mixed metal oxides. *J. Mater. Chem. A* **8**, 16421–16428 (2020).
23. Zhou, Z. *et al.* Carbon dioxide capture from open air using covalent organic frameworks. *Nature* **635**, 96–101 (2024).
24. Leonzio, G., Mwabonje, O., Fennell, P. S. & Shah, N. Environmental performance of different sorbents used for direct air capture. *Sustain. Prod. Consum.* **32**, 101–111 (2022).
25. Deutz, S. & Bardow, A. Life-cycle assessment of an industrial direct air capture process based on temperature–vacuum swing adsorption. *Nat. Energy* **6**, 203–213 (2021).
26. Bolisetty, S., Peydayesh, M. & Mezzenga, R. Sustainable technologies for water purification from heavy metals: review and analysis. *Chem. Soc. Rev.* **48**, 463–487 (2019).
27. Sievert, K., Schmidt, T. S. & Steffen, B. Considering technology characteristics to project future costs of direct air capture. *Joule* **8**, 979–999 (2024).
28. Kwon, H. T. *et al.* Aminopolymer-Impregnated Hierarchical Silica Structures: Unexpected Equivalent CO2 Uptake under Simulated Air Capture and Flue Gas Capture Conditions. *Chem. Mater.* **31**, 5229–5237 (2019).
29. Anderson, B. A., Shimoni, E., Liardon, R. & Labuza, T. P. The diffusion kinetics of carbon dioxide in fresh roasted and ground coffee. *J. Food Eng.* **59**, 71–78 (2003).